# Macrophage transactivation for chemokine production identified as a negative regulator of granulomatous inflammation using agent-based modeling.

Daniel Moyo[1,2], Lynette Beattie[1*], Paul S Andrews[3], John W J Moore[1], Jon Timmis[3], Amy Sawtell[1], Stefan Hoehme[4], Adam T. Sampson[5], Paul M Kaye[1]

[1.] Centre for Immunology and Infection, Department of Biology and Hull York Medical School, University of York, UK.

[2.] Department of Computer Science, University of York, UK.

[3.] Department of Electronics, University of York, UK and SimOmics Ltd, York. U.K.

[4.] Institute for Computer Science, University of Leipzig, Germany

[5.] Division of Computing and Mathematics, Abertay University, Dundee, UK.

*Current address: Doherty Institute, University of Melbourne, Australia.

**Key words:** Kupffer cells**;** granulomas; inflammation; *Leishmania*; NKT cells; agent-based modeling; computational immunology; liver

**Abstract**

Cellular activation *in trans* by interferons, cytokines and chemokines is a commonly recognized mechanism to amplify immune effector function and limit pathogen spread. However, an optimal host response also requires that collateral damage associated with inflammation is limited. This may be particularly so in the case of granulomatous inflammation, where an excessive number and / or excessively florid granulomas can have significant pathological consequences. Here, we have combined transcriptomics, agent-based modeling and *in vivo* experimental approaches to study constraints on hepatic granuloma formation in a murine model of experimental leishmaniasis. We demonstrate that chemokine production by non-infected Kupffer cells in the *Leishmania donovani*-infected liver promotes competition with infected KCs for available iNKT cells, ultimately inhibiting the extent of granulomatous inflammation. We propose trans-activation for chemokine production as a novel broadly applicable mechanism that may operate early in infection to limit excessive focal inflammation.

## Introduction

Immune responses are commonly initiated by localized infectious insult and multiple mechanisms have evolved to allow spread of host effector responses to meet the challenge of pathogen containment. In the late 1950's, seminal studies by Isaacs and Lindenmann defined how "interferons' amplified local cellular resistance following virus infection [1, 2]. A decade later, Mackaness described cross protective cellular immunity mediated via T cell cytokine-dependent macrophage activation [3]. More recently, cytokine-and chemokine- mediated amplification of host protective immunity has been described across a spectrum of responses driven by both innate lymphoid cells and via conventional T cells [4-9]. Whilst serving to eliminate pathogens more effectively, a potentially undesirable consequence of amplifying immune effector responses is immunopathology, collateral damage induced by an over-zealous drive towards inflammation. Hence, an equally impressive array of "regulatory" or "suppressive" mechanisms have been defined that serve to limit immunopathology, and that suggest an evolutionary balance between pathogen elimination and host survival [10-12].

Granulomatous inflammation represents an extreme form of focal inflammation, often initiated around pathogens or foreign bodies that pose a formidable challenge for immune clearance. Granulomas are a hallmark of the immunopathology of many human infectious diseases including tuberculosis [13, 14], schistosomiasis [15]and leishmaniasis [16]. Whilst granuloma formation may provide means for containment and be host beneficial, excessive granuloma formation, numerically or in terms of individual granuloma size can lead to severe pathological consequences. Hence,

mechanisms for limiting the exuberance of the granulomatous response through late acting regulatory pathways are also well described in the literature [17-20]. However, the question of whether additional regulatory mechanisms operate at the earliest stages of granuloma initiation and prevent or limit over-exuberant granuloma formation has not been previously addressed.

Experimental visceral leishmaniasis, resulting from infection of mice with the Kupffer cell (KC) tropic parasite *Leishmania donovani*, has provided a highly tractable tool to study the initiation of granulomatous pathology in the hepatic microenvironment. Following infection of mice with *L. donovani*, infected KCs transiently release the chemokines CCL1, CCL2 and CXCL10 in a T cell-independent manner, whereas sustained expression of CXCL10 is dependent upon IFNγ production by invariant NKT (iNKT) cells [21]. IFNγ production by iNKT cells is in turn costimulated by ligation of CD47 on NKT cells by signal regulatory protein alpha (SIRPα) expressed on KCs, providing positive feedback for sustained iNKT cell recruitment and KC activation [22]. A similar role for CXC chemokines in recruiting hepatic NKT cells has been observed in other models of liver infection / inflammation [23, 24]. For example, CXCL9 produced by KCs following infection with the bacterium *Borrelia burgdorferi* results in CXCR3-dependent clustering of NKT cells around infected KCs [25] whereas CXCR6 and its ligand CXCL16 regulate NKT cell accumulation in the liver during fibrosis [26]. Hence, early recruitment of "amplifier" cells such as NKT cells is a central and common theme of focal inflammation.

Examination of the kinetics of granulomatous inflammation in this model of visceral leishmaniasis suggests, however, that there may be inherent limitations imposed on the ability of the host to form hepatic granulomas. Notably, granuloma formation proceeds asynchronously, and even many weeks after infection, fully formed granulomas sit side by side with infected KCs that appear to have failed to stimulate an inflammatory focus [16, 27]. Here, we have combined transcriptional profiling and computational modeling to probe possible mechanisms that might underpin the asynchronous development of granulomas in this model. We demonstrate that KC chemokine production, contrary to expectations, is not restricted to infected cells alone, but spreads in trans to include uninfected KCs within the infected liver. Data generated using a novel agent based model (ABM) in which KCs and iNKT cells interact within a spatially constrained sinusoidal network suggest that the spreading of chemokine production to uninfected KCs limits the competitiveness of infected KCs in terms of their ability to attract iNKT cells and initiate granuloma formation. In silico experiments predicted that this competition could be overcome by increasing the number of available NKT cells, a prediction borne out in vivo. Hence, our data identify a new pathway that operates early in infection to limit excessive inflammation by introducing competition for a finite resource (i.e. iNKT cells) that is needed for granuloma initiation.

## Materials and Methods

*Mice and parasites.*

C57BL6 mice were obtained from Charles River (UK). mT/mG [28] and LysMcre [29] mice have been previously described. Mice were bred and housed under specific

pathogen-free conditions and used at 6-12 weeks of age. The tandom Tomato fluorescent protein expressing Ethiopian strain of *Leishmania donovani* (tdTom.LV9) [30] were maintained by serial passage in *Rag1*$^{-/-}$ mice. Amastigotes were isolated from infected spleens, and mice were infected with $3x10^7$ *L. donovani* amastigotes intravenously (i.v.) via the tail vein in 200µl of RPMI 1640 (GIBCO, UK). All animal procedures were approved by the University of York Animal Welfare and Ethical Review Board and carried out in accordance with UK Home Office license (PPL 60/4377).

*Microarray analysis*

As previously described [31], Kupffer cells were flow sorted (on the basis of SSC/FSC and expression of CRIg, Gr-1 and F4/80) from naive mice and from infected mice and KCs from infected mice were further sorted (on the basis of TdTomato expression) into those containing amastigotes ("infected") and those that did not ("inflamed"). A total of 64 mice were used in the microarry study, in four independent infection experiments. RNA was isolated, amplified and equal amounts were assayed using Agilent SurePrint G3 Gene Expression 8x60 Microarray chips. Scanned data were normalized ($80^{th}$ percentile) and gene expression data analysed using Genespring v9. Differentially expressed (DE) genes were defined using a false discovery rate (FDR) of 5%. Source data is accessible from EBI Array Express (E-MEXP-3877) and methodology for subsequent data analysis is described in further detail elsewhere [31].

*Histological Analysis.*

Mice were treated with 1μg recombinant IL-15 (BioLegend) intravenously and infected 3 days later. Four days post-infection, mice livers were extracted, weighed then placed into 2% PFA in PBS for 2 hours, then 30% sucrose in PBS overnight. Tissues were then embedded in Optimal Cutting Temperature (OCT)(Sakura) and stored at -70°C until use. 10μm cryosections were fixed and labeled with Alexa647 or Alexa488 conjugated F4/80 (eBioscience) and DAPI (Invitrogen) to visualize KCs and cell nuclei respectively. Images were captured as 0.81μm optical slices using a LSM510 confocal microscope (Zeiss). Blinded slides were imaged to score the percentage of infected foci having formed a distinct inflammatory focus (greater than 15 cells), with imaging fields selected via tdTomato expression.

*Flow Cytometry.*

Livers were homogenized and mononuclear cells prepared as previously described [30]. Cells were incubated with anti-CD16/32 and then labeled with NK1.1, CD3, B220 and CD1d tetramer (a kind gift from V. Cerundulo) to identify T, NK and NKT cells. Samples were analyzed using a CyAn flow cytometer with Summit software (DAKO). Autofluorescent events and dead cells were excluded from analysis by gating on unused fluorescent channels and LIVE/DEAD fixable dead cell stain (Invitrogen) respectively.

*Parameterizing and Calibrating the Simulation.*

A full summary of the biological data available that was used to calibrate the simulation is listed in **Table S1**. The entire list of baseline simulation parameters is found in **Tables S3**. Full details of parameterization and calibration of the simulation are provided in the **Supplemental Experimental Procedures**.

*Statistical Analysis*.

When quantifying granulomas, experimental data are expressed as mean ± SEM for each group of 5 mice from two independent experiments, and statistical analyses performed using two-tailed paired Student t-tests. All tests used 95% confidence intervals. Simulation data non-normality was determined using the D'Agostino and Pearson test, and non-normal simulation data was analyzed using either Wilcoxon signed-rank or Kolmogorov-Smirnov tests where appropriate. Aleatory analysis was used to determine the minimum number of simulation results required to mitigate stochastic uncertainty (see **Figure S4**). Latin-hypercube sensitivity analysis was facilitated by using the Spartan tool for understanding uncertainty in simulations [32].

## Results

*Chemokine production by KCs in mice infected with L. donovani*

Both chemokines and iNKT cells are central to the initiation of granulomatous inflammation following *L. donovani* infection. In order to gain insight into the production of chemokines involved in KC-directed recruitment of NKT cells, we used transcriptional profiling of KCs isolated from mice infected with *L. donovani* as

previously described [31]. Following infection of mice with Td-tomato transgenic *L. donovani*, approx. 20% of the KC population are infected with amastigotes. We isolated KCs from infected mice and sort purified these KCs on the basis of whether they contained intracellular amastigotes ("infected') or not (herein referred to as "inflamed" to denote their exposure to inflammatory signals *in vivo*) [31]. As shown in **Figure 1A**, KCs from infected mice expressed a variety of chemokines when compared to KCs isolated from naïve mice. At 2h post infection (p.i.), enhanced accumulation of mRNAs for *Cxcl1*, *Cxcl2*, *Cxcl3* and *Cxcl5*, as well as *Ccl3* and *Ccl4*, was evident (determined as differentially expressed using a 5% FDR). This transcriptional response was transient, in keeping with previous studies at the level of whole liver tissue [21]. Rapid secretion of chemokines in response to *L. donovani* infection can also be inferred from studies in which G-protein coupled receptor signaling was abrogated by pertussis toxin [22]. A suite of inducible chemokines, including *Cxcl9*, *Cxcl10*, *Ccl8* and *Ccl12* showed enhanced mRNA accumulation at 12h p.i. (at a 5% FDR), again in keeping with data in whole liver and with previously published data indicating the production of IFNγ by iNKT cells during early *L. donovani* infection (e.g. Figure 2 in reference 22). For example, qRT-PCR demonstrated sustained and elevated *Cxcl10* at 24h p.i. [33]. Similarly, transcriptional profiling of the livers of infected BALB/c mice (n=4-5 per time point) indicates sustained elevation of *Cxcl9* ($Log_2FC$ compared to controls of 5.25, 5.14, 5.34 and 4.74 for days 15, 21, 36 and 42 p.i. respectively; FDR 0.05, $p<0.05$) and *Cxcl10* ($Log_2FC$ of 4.84, 4.92, 5.36 and 4.55, respectively; Ashwin et al, manuscript in preparation). Strikingly, there was little difference to discriminate the chemokine response of infected vs. inflamed KCs, although we cannot rule out different degrees of post transcriptional regulation of chemokine secretion in infected vs. inflamed KCs

198 [34]. Collectively, our data suggest that although initiated by infection, production of
199 chemokines rapidly spreads in trans throughout the liver KC network.

200

201 Chemokine induction by infected cells is thought to provide a means for focal
202 inflammation, the recruitment of additional leucocytes in an ordered manner being
203 essential for granuloma formation and the ultimate activation of macrophage host
204 defense mechanisms. However, given this argument, these data appear
205 counterintuitive. In order to try to understand how transactivation for chemokine
206 production might influence the generation of focal inflammation, and given the
207 absence of tools to selectively and directly manipulate chemokine production by
208 infected vs. uninfected KCs *in vivo*, we adopted an *in silico* experimental approach
209 conducive to testing a variety of different hypotheses (**Figure 1B and C**).

210

211 *An agent-based model of the hepatic sinusoidal microenvironment.*

212 Agent based models, where rule-driven "agents" can represent a cell or lower-scale
213 entities of interest, are naturally suited to simulating inflammation in a spatially
214 constrained environment [35-37]. To construct this environment, we used published
215 3D data describing the overall size of lobules, the average non-branched sinusoid
216 length, and the branching angles between sinusoids [38] as the basis for developing a
217 novel algorithm to generate statistically realistic liver lobule sections similar to that
218 reported recently [39]. A range of quasi-2D sinusoidal network structures, where
219 each structure can be considered as a slice through a 3D lobule, was created using a
220 multi-stage generative algorithm augmented with these data [38] (**Figure 2A**, **Movie**

**S1**, **Figure S1A-D** and **Table S1** and **Supplementary Experimental Procedures**). The resulting networks **(Figure 2B)**, represented as graphs of nodes connected by edges, serve as discrete spatial simulation environments that mimic the sinusoidal structure observed in live mice imaged by 2-photon intra-vital microscopy in (mT/mG x lysMcre)$_{F1}$, as previously described [30] (**Figure 2A vs. 2C**). Analysis (by Pearson correlation coefficients and Kolmogorov-Smirnov tests) using 10 independently generated structures indicated that variance in structure *per se* had minimal impact on the results of subsequent simulations (see below).

We defined where and how cellular interactions were allowed to occur within our simulation environment based on 3 different types of network node: periportal nodes, located at the peripheries of the structure allow NKT cells to enter and exit the simulated lobule section; regular-nodes, capable of holding a single KC and any number of NKT cells; and a single centrilobular-node, representing the central vein where NKT cells could exit the structure. Only NKT cells were capable of movement within the structure. KCs remain immobile, as reported in early stages of infection with *B. bugdorferi* [25], BCG [40] and *L. donovani* [30]. Our KC placement algorithm distributes KCs in periportal, midzonal and centrilobular locations in a ratio of 4:3:3, based on [41, 42]. As centrilobular KCs have reduced phagocytic capability compared to periportal KCs [41], the distribution of infected KCs in our simulation is 65% periportal, 25% midzonal and 10% centrilobular for the purposes of experimentation.

A detailed description of the model and key assumptions is provided in the **Supplemental Experimental Procedures and Tables S2 and S3**. State diagrams written in the Unified Modeling Language that illustrate the behaviour associated with KCs and NKT cells are provided in **Figure S2**. Briefly, mechanisms of cellular attraction and retention were modeled generically, since the precise function, functional overlap, and interaction between distinct chemokines has yet to be fully elucidated. For the purposes of the current abstraction, we refer to the chemokines as attractive and retentive, being independent and quantitatively distinct and with discrete areas of influence. The simulation was constructed to allow both a minimum and a maximum diffusion distance to be parameterized for all chemo-attractants produced by KCs. NKT cells traverse the sinusoidal network at 10-20μm/min with a random walk behavior [25], with no enforcement of directionality unless under the attractive influence of KC-derived chemokines. Strength of attraction is modeled as a function of distance from the source KC. Upon interaction with infected KCs, NKT cells produce IFNγ (as a representation of all macrophage-activating cytokines) following cognate receptor engagement [22], facilitating KC activation and NKT cell arrest [25, 43]. Our previous data on SIRPα-CD47 has suggested that cognate receptor-ligand interactions also regulate NKT cell retention on infected KCs, with the induced expression of SIRPα after infection being preferentially but not exclusively observed on infected KCs [22]. In our model, this interaction is used to represent a cognate retention signal, but this reflects an abstraction of what may be potentially much more complex interactions. The amplification of KC derived attractive chemokines through this process can lead to the accumulation of multiple NKT cells at a given KC (referred to here as "inflammatory foci"). It is assumed that through the sum of all KC-NKT cell interactions within an inflammatory focus, a

threshold for granuloma formation and the subsequent recruitment of additional leucocytes associated with maturing granulomas (including B cells, T cells, monocytes and NK cells) is reached, but these cells and processes are not explicitly modeled. We have also not modeled the ultimate microbicidal activity of these granulomas.

*Parasite Induced Activation of Infected KCs with/without Bystander Chemokine production by Uninfected KCs.*

Two experimental scenarios were devised to investigate the influence of varying both infected and inflamed KC function. Scenario 1 (**Figure 1B**) was constructed to restrict chemokine production to infected KCs only, and scenario 2 (**Figure 1C**) to investigate the impact of transactivation of KC for chemokine production. As KC activation of NKT cells is optimal in the presence of cognate interactions [22], our model assumes these are a requirement for retention; hence only infected KCs can generate stable inflammatory foci, and these foci, for the purposes of the model, are composed only of NKT cells and KCs. In contrast, inflamed KCs in scenario 2 might act as potential competitors for available NKT cells, being able to attract but not retain them. Although this model can be used to probe a variety of different potential questions related to the initiation of granuloma formation (see Discussion), we focus here on a factorial analysis that involved simultaneously modifying the simulation parameters related to chemokine diffusion distance, time required to activate KCs, and time for KCs to reach maximal chemokine production.

292 Firstly, we quantified the influence of distance from effect on attraction. Factorial
293 analysis, modifying the maximum diffusion distance of chemokine, showed that
294 greater chemokine diffusion distance leads to increased percentages of infected KCs
295 forming inflammatory foci in both scenarios (**Figure 1B** and **C**), whether those foci
296 were qualified as containing 4, 6 or 8 NKT cells. However, our simulation predicted
297 diminishing returns when increasing maximum diffusion past ~120μm (**Figure S1E**).
298 Thus, significant differences (P=≤0.001) were observed when comparing the
299 frequency of inflammatory foci that resulted from each increase in diffusion distance
300 against the previous distance (e.g. 20μm-30μm: P=0.001216, 30μm-40μm:
301 P=0.000019). However, when increasing from 120μm-130μm and beyond, the
302 increase in inflammatory foci was not significant (P=0.312). Interestingly, this tipping
303 point is close to the ~100μm reported as the distance of a functional chemokine
304 gradient *in vivo* [44]. These results suggest that if it were possible to selectively
305 increase chemokine diffusion via increased production (or other means) by infected
306 KCs compared to inflamed KCs, or conversely decrease chemokine diffusion by
307 inflamed KCs, infected KCs would gain competitive advantage in terms of attracting
308 NKT cells.

309

310 We next compared our two experimental scenarios in terms of total stimulation time
311 (i.e. a measure of activation) received by the entire infected KC population, and the
312 frequency of inflammatory foci formed associated with that population. **Figure 3A**
313 illustrates a response curve for scenario 1 showing the total stimulation time received
314 by all infected KCs, across a range of the two main parameters that determine KC
315 activation dynamics – the time required to activate KCs and the duration KCs remain

316 activated. When comparing this response landscape of scenario 1 with that generated
317 in scenario 2 (**Figure 3C**), there was a marked reduction in stimulation time received
318 overall by infected KCs in scenario 2 compared to scenario 1. This trend is also
319 observable when comparing the percentage of inflammatory foci, whether qualified at
320 8 NKT cells (**Figure 3B** for scenario 1 and **Figure 3D** for scenario 2) or at 4 or 6
321 NKT cells (data not shown).

322

323 Together, these results demonstrate that in comparison to chemokine production
324 restricted to infected KCs, additional chemokine production by inflamed KC
325 generates a less focused inflammatory response, measured either by frequency of
326 infected KC that form inflammatory foci, or by stimulation time received by infected
327 KCs. This result most likely reflects the liver lobule becoming saturated with
328 attractive chemokines derived from both inflamed and infected KCs in scenario 2,
329 reducing the competitiveness of infected KCs to selectively recruit NKT cells. In
330 other words, chemokine production by inflamed KC acts in a negative immune
331 regulatory manner, limiting the extent of the inflammatory response around infected
332 KCs.

333

334 *Increasing NKT Cell Numbers Overcomes Bystander Regulation.*

335 We then investigated how modifying the target of this competition affected the
336 quantity and quality of inflammatory foci generated. We hypothesized that altering
337 NKT cell frequency might result in either i) similarly abundant foci, but with each
338 being more substantive in terms of NKT cellularity, or ii) increased numbers of

339 inflammatory foci, thus overcoming the competitive effect of bystander chemokine
340 production by inflamed KCs (**Figure 4A**). Our simulation results showed that
341 increasing NKT cell numbers above the calibrated value lead to significant increases
342 in the frequency of inflammatory foci in scenario 1, a result that would be expected.
343 Strikingly, an increase in frequency of inflammatory foci was also observed to be the
344 case for scenario 2, regardless of how we qualified focus size (**Figure 4B**). For
345 example, with an increase in NKT cell availability of 2-fold, the number of
346 inflammatory foci increased 1.5-fold, whereas increasing NKT cells by 3-fold
347 doubled the frequency of inflammatory foci.

348

349 To test whether this predictive *in silico* data was also borne out *in vivo*, we treated
350 mice for 3 days with recombinant IL-15 to induce increased NKT cell proliferation
351 and survival [45] and then infected these mice with *L. donovani* and scored early
352 granuloma formation. In uninfected mice, IL-15 treatment resulted in increased
353 numbers of NKT cells (including CD1d restricted NKT cells), NK cells, and T cells
354 (**Figure 4C-E** and **Figure S3A-D**). In infected mice, all cell types were already
355 increased in number compared to naïve mice, and the effect of IL-15 pre-treatment
356 was limited to an increase in the number of NKT cells (**Figure 4C**). Similarly, IL-15
357 pre-treatment had no effect on the relative frequency of NK cells and T cells (**Figure**
358 **S3B-C**) but resulted in an increase in the relative frequency of NKT cells (from 15.0
359 ± 0.1% to 17.36 ± 0.8%; n=10; P=0.0043; **Figure S3E**).

360

361 To ensure that we were scoring a biologically relevant histopathological response,
362 whilst minimizing potential longer terms effects of rIL-15 treatment, we chose to

score the granulomas early in their development (day 4 p.i.) and define these as accumulations of 15 or more cells formed around an infected KC (not discriminating between NKT cells or other mononuclear cells). Although there was significant heterogeneity in size of these granulomas (**Figure 4G-H**), we found that the frequency of infected KCs that formed distinct granulomas was increased ~1.5 fold in mice pre-treated with IL-15 and which had a higher number of NKT cells in the liver at the time of infection (P=0.0038; **Figure 4F**). Thus, treatment of mice with rIL-15, even under conditions where the increase in NKT cell number is relatively modest, leads to a significant enhancement in the frequency of infected KCs that can provide a nidus for granuloma formation.

## Discussion

Granulomas represent a specialized form of inflammation that allows for the focal delivery of host effector responses and / or containment of pathogen products. Whilst generally considered host beneficial, excessive granuloma formation may have significant pathological consequences. Here, we provide evidence that chemokine-dependent competition between infected and uninfected KCs for iNKT cells in the hepatic microenvironment acts as a natural attenuator of granuloma formation.

In models of experimental visceral leishmaniasis, granuloma formation is asynchronous, limiting the extent of hepatic inflammation, but also delaying parasite clearance [16, 27]. A variety of different models could explain why isolated infected KCs can be found at times when other infected KCs are engaged in a fully mature

386 granulomatous response. In a model of *Mycobacterium marinarum*-induced
387 granulomas in zebrafish, macrophage migration out of the granuloma has been
388 observed [14, 46], and it is possible that infected KCs leave granulomas in mice
389 infected with *L. donovani*. However, in both *L. donovani*-induced granulomas [30]
390 and BCG-induced granulomas [40, 47] in immunocompetent mice, KCs appear to
391 retain their characteristic lack of motility. Alternatively, there may be heterogeneity
392 in KCs, a subset being more efficient in promoting granulomatous inflammation.
393 Although we had previously modeled this possibility using an early version of our
394 ABM [48], our recent studies evaluating differences between yolk-sac derived and
395 bone marrow-derived KC indicate that both are competent to form granulomas and
396 participate effectively in this response [49]. A further possibility is that granuloma
397 formation is rate limited by the availability of key amplifier cells. Experimental data
398 to date indicates that iNKT cells play this role in experimental visceral leishmaniasis
399 [22, 33, 50, 51], though we do not discount a role for other more recently identified
400 innate lymphoid cells [52, 53].

401

402 Through transcriptional profiling, we demonstrated that both inflamed and infected
403 KCs produce a variety of inducible chemokines able to attract NKT cells, suggesting
404 the possibility that uninfected as well as infected KCs could compete for this
405 resource. However, as neither the mechanisms that regulate this transactivation nor
406 experimental means to selectively regulate chemokine production by KCs are
407 currently available, we adopted a computational approach to further explore this
408 hypothesis. ABMs are well-suited towards studying tissue and cellular level
409 inflammation [35-37]. In constructing our ABM, we developed a novel algorithm for

creating virtual sinusoidal networks that are visually representative of liver lobule sections, being defined by published statistics that captured the length between central vein and portal triad, average lengths of non-branched sinusoids and sinusoid branch angles [38]. This represents an improvement on similar work [39]. Our algorithm was not intended to produce a fully realistic whole lobule structure, but rather we were interested only in developing suitable quasi-2D vascular networks within liver lobules to provide an environment for the cellular and chemokine "agents" contained in the model. Similarly, whilst our ABM contained only three cellular agents (infected and inflamed KCs and NKT), this abstraction was nevertheless sufficient to probe previously inaccessible aspects of the underlying biology.

Our *in silico* results predicted that chemokine diffusion plays an important role in regulating the formation of inflammatory foci around infected KCs, though there are diminishing returns as a result of increased competition when lobules become flooded with chemokines. Subsequently, our model predicted an intuitive, but nonetheless previously unreported mechanism by which the production of NKT cell-attractive chemokines by inflamed KCs dampens the overall inflammatory response in the liver microenvironment, reducing the activation received by infected KCs. Our *in silico* data also predicted that this competition could be overcome by increasing the availability of NKT cells, and we were able to confirm that granuloma frequency can indeed be increased *in vivo* by increasing NKT cell numbers using rIL-15. The relationship between availability of NKT cells and an increase in the frequency of infected KCs generating granulomas has not previously been demonstrated.

434 Natural killer T (NKT) cells represent a potent therapeutic target in a variety of
435 clinical settings, due to their immune adjuvant function and production of various
436 effector cytokines [54-57]. Protective immunity associated with NKT cell activation
437 has been reported in several disease settings. For example, Vα14 NKT cells activated
438 by α-galactosylceramide (α-GalCer) have been shown to inhibit the development of
439 malaria parasites in mice [58]. Similarly, in a murine model of *Mycobacterium*
440 *tuberculosis* infection, α-GalCer induced activation of NKT cells was associated with
441 reduced bacterial loads, tissue injury, and improved mouse survival [59]. Conversely,
442 NKT cells have been implicated as key drivers of liver inflammation such as chronic
443 liver injury [26]. Although our results suggest that in leishmaniasis the initiation of
444 granulomatous inflammation can be enhanced by increasing the availability of NKT
445 cells, further long-term studies would be required to determine whether the host
446 protective advantages of this intervention outweigh any possible pathological
447 consequences.

448

449 It is important to recognize that our model has been developed to address early events
450 in granuloma formation and does not take into account the potential for diversity in
451 granuloma form and function, including variations in microbicidal activity. These
452 may be regulated via other aspects of the immune response that develop over time,
453 and more complex models have been developed to address some of these issues [60].
454 Redundancy of immune regulatory pathways is a common finding and it is possible
455 that other mechanisms come into play at later stages of granuloma evolution that
456 affects the ability of Kupffer cells to recruit inflammatory cells and initiate granuloma
457 formation. The kinetics of chemokine production is also likely to be highly dynamic,

458 though in respect of CXCL9 and CXCL10, long term transcriptomic profiling
459 indicates that expression of these IFNγ-inducible chemokines is sustained for at least
460 45 days post infection (Ashwin et. al., unpublished).

461 In summary, our data argue that chemokine production by uninfected trans-activated
462 KCs provides an example of a novel negative regulatory mechanism to limit the
463 impact of over-zealous inflammatory responses that might otherwise lead to excess
464 tissue pathology. Further studies to evaluate this hypothesis in a broader context of
465 inflammation are clearly warranted.

466

467 **Acknowledgements**

468 This work was supported by grants from The Wellcome Trust and the British Medical
469 Research Council (to PMK), and the Engineering and Physical Science Research
470 Council (to JT and PSA). JT is partly funded by the Royal Society. The authors thank
471 Vincenzo Cerundolo for providing the CD1d tetramers.

472

473 **Author conflict of interest statement**

474 JT is Director of SimOmics Ltd; PSA is employed by SimOmics Ltd; all other authors
475 declare no conflict of interest.

476

477 **Author Contributions**

478 DM, PSA, JT, LB and PMK designed the simulation model. DM implemented the
479 simulation model. LB and PMK designed the experimental study. DM, JWM, LB and
480 AS performed experimental studies. SH provided data and input on model

development. PSA and ATS designed and implemented the algorithm for the generation of the artificial sinusoid structures. DM, LB, PSA, JT and PMK analyzed the data and wrote the manuscript.

## References


1. Isaacs A, Lindenmann J. Virus interference. I. The interferon. Proc R Soc Lond B Biol Sci. 1957;147(927):258-67. Epub 1957/09/12. PubMed PMID: 13465720.

2. Isaacs A, Lindenmann J, Valentine RC. Virus interference. II. Some properties of interferon. Proc R Soc Lond B Biol Sci. 1957;147(927):268-73. Epub 1957/09/12. PubMed PMID: 13465721.

3. Mackaness GB. The influence of immunologically committed lymphoid cells on macrophage activity in vivo. J Exp Med. 1969;129(5):973-92. Epub 1969/05/01. PubMed PMID: 4976110; PubMed Central PMCID: PMCPMC2138649.

4. Chu T, Tyznik AJ, Roepke S, Berkley AM, Woodward-Davis A, Pattacini L, et al. Bystander-activated memory CD8 T cells control early pathogen load in an innate-like, NKG2D-dependent manner. Cell Rep. 2013;3(3):701-8. Epub 2013/03/26. doi: 10.1016/j.celrep.2013.02.020. PubMed PMID: 23523350; PubMed Central PMCID: PMCPMC3628815.

5. Griffith JW, Sokol CL, Luster AD. Chemokines and chemokine receptors: positioning cells for host defense and immunity. Annu Rev Immunol. 2014;32:659-702. Epub 2014/03/25. doi: 10.1146/annurev-immunol-032713-120145. PubMed PMID: 24655300.

6. Lertmemongkolchai G, Cai G, Hunter CA, Bancroft GJ. Bystander activation of CD8+ T cells contributes to the rapid production of IFN-gamma in response to bacterial pathogens. J Immunol. 2001;166(2):1097-105. Epub 2001/01/06. PubMed PMID: 11145690.

7. Mantovani A, Sica A, Sozzani S, Allavena P, Vecchi A, Locati M. The chemokine system in diverse forms of macrophage activation and polarization. Trends

510 Immunol. 2004;25(12):677-86. Epub 2004/11/09. doi: 10.1016/j.it.2004.09.015.
511 PubMed PMID: 15530839.
512 8. Polley R, Sanos SL, Prickett S, Haque A, Kaye PM. Chronic Leishmania
513 donovani infection promotes bystander CD8+-T-cell expansion and heterologous
514 immunity. Infect Immun. 2005;73(12):7996-8001. Epub 2005/11/22. doi:
515 10.1128/IAI.73.12.7996-8001.2005. PubMed PMID: 16299292; PubMed Central
516 PMCID: PMCPMC1307086.
517 9. Tough DF, Borrow P, Sprent J. Induction of bystander T cell proliferation by
518 viruses and type I interferon in vivo. Science. 1996;272(5270):1947-50. Epub
519 1996/06/28. PubMed PMID: 8658169.
520 10. Graham AL, Allen JE, Read AF. Evolutionary causes and consequences of
521 immunopathology. Annual review of Ecology, Evolution and Systematics.
522 2005;36:373-97. doi: 10.1146/annurev.ecolsys.36.102003.152622.
523 11. Mills KH. Regulatory T cells: friend or foe in immunity to infection? Nat Rev
524 Immunol. 2004;4(11):841-55. Epub 2004/11/02. doi: 10.1038/nri1485. PubMed
525 PMID: 15516964.
526 12. Sorci G, Cornet S, Faivre B. Immune evasion, immunopathology and the
527 regulation of the immune system. Pathogens. 2013;2(1):71-91. Epub 2013/01/01. doi:
528 10.3390/pathogens2010071. PubMed PMID: 25436882; PubMed Central PMCID:
529 PMCPMC4235712.
530 13. Dorhoi A, Kaufmann SH. Perspectives on host adaptation in response to
531 Mycobacterium tuberculosis: modulation of inflammation. Semin Immunol.
532 2014;26(6):533-42. Epub 2014/12/03. doi: 10.1016/j.smim.2014.10.002. PubMed
533 PMID: 25453228.

14. Pagan AJ, Ramakrishnan L. Immunity and Immunopathology in the Tuberculous Granuloma. Cold Spring Harbor perspectives in medicine. 2015;5(9). doi: doi: 10.1101/cshperspect.a018499. .

15. Hams E, Aviello G, Fallon PG. The schistosoma granuloma: friend or foe? Front Immunol. 2013;4:89. Epub 2013/04/19. doi: 10.3389/fimmu.2013.00089. PubMed PMID: 23596444; PubMed Central PMCID: PMCPMC3625856.

16. Kaye PM, Beattie L. Lessons from other diseases: granulomatous inflammation in leishmaniasis. Semin Immunopathol. 2016;38(2):249-60. Epub 2015/12/19. doi: 10.1007/s00281-015-0548-7. PubMed PMID: 26678994; PubMed Central PMCID: PMCPMC4779128.

17. Lundy SK, Lukacs NW. Chronic schistosome infection leads to modulation of granuloma formation and systemic immune suppression. Front Immunol. 2013;4:39. Epub 2013/02/23. doi: 10.3389/fimmu.2013.00039. PubMed PMID: 23429492; PubMed Central PMCID: PMCPMC3576626.

18. Maroof A, Beattie L, Zubairi S, Svensson M, Stager S, Kaye PM. Posttranscriptional regulation of Il10 gene expression allows natural killer cells to express immunoregulatory function. Immunity. 2008;29(2):295-305. Epub 2008/08/15. doi: 10.1016/j.immuni.2008.06.012. PubMed PMID: 18701085; PubMed Central PMCID: PMCPMC2656759.

19. Mentink-Kane MM, Cheever AW, Thompson RW, Hari DM, Kabatereine NB, Vennervald BJ, et al. IL-13 receptor alpha 2 down-modulates granulomatous inflammation and prolongs host survival in schistosomiasis. Proc Natl Acad Sci U S A. 2004;101(2):586-90. Epub 2003/12/31. doi: 10.1073/pnas.0305064101. PubMed PMID: 14699044; PubMed Central PMCID: PMCPMC327191.

558 20. Owens BM, Beattie L, Moore JW, Brown N, Mann JL, Dalton JE, et al. IL-10-
559 producing Th1 cells and disease progression are regulated by distinct CD11c(+) cell
560 populations during visceral leishmaniasis. PLoS Pathog. 2012;8(7):e1002827. Epub
561 2012/08/23. doi: 10.1371/journal.ppat.1002827. PubMed PMID: 22911108; PubMed
562 Central PMCID: PMCPMC3406093.
563 21. Cotterell SE, Engwerda CR, Kaye PM. Leishmania donovani infection
564 initiates T cell-independent chemokine responses, which are subsequently amplified
565 in a T cell-dependent manner. Eur J Immunol. 1999;29(1):203-14. Epub 1999/02/05.
566 doi: 10.1002/(SICI)1521-4141(199901)29:01<203::AID-
567 IMMU203>3.0.CO;2-B. PubMed PMID: 9933102.
568 22. Beattie L, Svensson M, Bune A, Brown N, Maroof A, Zubairi S, et al.
569 Leishmania donovani-induced expression of signal regulatory protein alpha on
570 Kupffer cells enhances hepatic invariant NKT-cell activation. Eur J Immunol.
571 2010;40(1):117-23. Epub 2009/10/31. doi: 10.1002/eji.200939863. PubMed PMID:
572 19877019; PubMed Central PMCID: PMCPMC2909397.
573 23. Gupta G, Bhattacharjee S, Bhattacharyya S, Bhattacharya P, Adhikari A,
574 Mukherjee A, et al. CXC chemokine-mediated protection against visceral
575 leishmaniasis: involvement of the proinflammatory response. J Infect Dis.
576 2009;200(8):1300-10. Epub 2009/09/12. doi: 10.1086/605895. PubMed PMID:
577 19743920.
578 24. Sato T, Thorlacius H, Johnston B, Staton TL, Xiang W, Littman DR, et al.
579 Role for CXCR6 in recruitment of activated CD8+ lymphocytes to inflamed liver. J
580 Immunol. 2005;174(1):277-83. Epub 2004/12/22. PubMed PMID: 15611250.
581 25. Lee WY, Moriarty TJ, Wong CH, Zhou H, Strieter RM, van Rooijen N, et al.
582 An intravascular immune response to Borrelia burgdorferi involves Kupffer cells and

583 iNKT cells. Nat Immunol. 2010;11(4):295-302. Epub 2010/03/17. doi:
584 10.1038/ni.1855. PubMed PMID: 20228796; PubMed Central PMCID:
585 PMCPMC5114121.
586 26. Wehr A, Baeck C, Heymann F, Niemietz PM, Hammerich L, Martin C, et al.
587 Chemokine receptor CXCR6-dependent hepatic NK T Cell accumulation promotes
588 inflammation and liver fibrosis. J Immunol. 2013;190(10):5226-36. Epub 2013/04/19.
589 doi: 10.4049/jimmunol.1202909. PubMed PMID: 23596313.
590 27. Murray HW. Tissue granuloma structure-function in experimental visceral
591 leishmaniasis. Int J Exp Pathol. 2001;82(5):249-67. Epub 2001/11/13. PubMed
592 PMID: 11703536; PubMed Central PMCID: PMCPMC2517779.
593 28. Muzumdar MD, Tasic B, Miyamichi K, Li L, Luo L. A global double-
594 fluorescent Cre reporter mouse. Genesis. 2007;45(9):593-605. Epub 2007/09/18. doi:
595 10.1002/dvg.20335. PubMed PMID: 17868096.
596 29. Clausen BE, Burkhardt C, Reith W, Renkawitz R, Forster I. Conditional gene
597 targeting in macrophages and granulocytes using LysMcre mice. Transgenic Res.
598 1999;8(4):265-77. Epub 2000/01/06. PubMed PMID: 10621974.
599 30. Beattie L, Peltan A, Maroof A, Kirby A, Brown N, Coles M, et al. Dynamic
600 imaging of experimental Leishmania donovani-induced hepatic granulomas detects
601 Kupffer cell-restricted antigen presentation to antigen-specific CD8 T cells. PLoS
602 Pathog. 2010;6(3):e1000805. Epub 2010/03/20. doi: 10.1371/journal.ppat.1000805.
603 PubMed PMID: 20300603; PubMed Central PMCID: PMCPMC2837408.
604 31. Beattie L, d'El-Rei Hermida M, Moore JW, Maroof A, Brown N, Lagos D, et
605 al. A transcriptomic network identified in uninfected macrophages responding to
606 inflammation controls intracellular pathogen survival. Cell Host Microbe.

607 2013;14(3):357-68. Epub 2013/09/17. doi: 10.1016/j.chom.2013.08.004. PubMed
608 PMID: 24034621; PubMed Central PMCID: PMCPMC4180915.
609 32. Alden K, Read M, Timmis J, Andrews PS, Veiga-Fernandes H, Coles M.
610 Spartan: a comprehensive tool for understanding uncertainty in simulations of
611 biological systems. PLoS Comput Biol. 2013;9(2):e1002916. Epub 2013/03/08. doi:
612 10.1371/journal.pcbi.1002916. PubMed PMID: 23468606; PubMed Central PMCID:
613 PMCPMC3585389.
614 33. Svensson M, Zubairi S, Maroof A, Kazi F, Taniguchi M, Kaye PM. Invariant
615 NKT cells are essential for the regulation of hepatic CXCL10 gene expression during
616 Leishmania donovani infection. Infect Immun. 2005;73(11):7541-7. Epub
617 2005/10/22. doi: 10.1128/IAI.73.11.7541-7547.2005. PubMed PMID: 16239557;
618 PubMed Central PMCID: PMCPMC1273891.
619 34. Fan J, Heller NM, Gorospe M, Atasoy U, Stellato C. The role of post-
620 transcriptional regulation in chemokine gene expression in inflammation and allergy.
621 Eur Respir J. 2005;26(5):933-47. Epub 2005/11/03. doi:
622 10.1183/09031936.05.00120204. PubMed PMID: 16264057.
623 35. An G. Concepts for developing a collaborative in silico model of the acute
624 inflammatory response using agent-based modeling. J Crit Care. 2006;21(1):105-10;
625 discussion 10-1. Epub 2006/04/18. doi: 10.1016/j.jcrc.2005.11.012. PubMed PMID:
626 16616634.
627 36. An G, Christley S. Addressing the translational dilemma: dynamic knowledge
628 representation of inflammation using agent-based modeling. Crit Rev Biomed Eng.
629 2012;40(4):323-40. Epub 2012/11/13. PubMed PMID: 23140123.
630 37. Moore JW, Moyo D, Beattie L, Andrews PS, Timmis J, Kaye PM. Functional
631 complexity of the Leishmania granuloma and the potential of in silico modeling.

632 Front Immunol. 2013;4:35. Epub 2013/02/21. doi: 10.3389/fimmu.2013.00035.
633 PubMed PMID: 23423646; PubMed Central PMCID: PMCPMC3573688.
634 38. Hoehme S, Brulport M, Bauer A, Bedawy E, Schormann W, Hermes M, et al.
635 Prediction and validation of cell alignment along microvessels as order principle to
636 restore tissue architecture in liver regeneration. Proc Natl Acad Sci U S A.
637 2010;107(23):10371-6. Epub 2010/05/21. doi: 10.1073/pnas.0909374107. PubMed
638 PMID: 20484673; PubMed Central PMCID: PMCPMC2890786.
639 39. Wambaugh J, Shah I. Simulating microdosimetry in a virtual hepatic lobule.
640 PLoS Comput Biol. 2010;6(4):e1000756. Epub 2010/04/28. doi:
641 10.1371/journal.pcbi.1000756. PubMed PMID: 20421935; PubMed Central PMCID:
642 PMCPMC2858695.
643 40. Egen JG, Rothfuchs AG, Feng CG, Winter N, Sher A, Germain RN.
644 Macrophage and T cell dynamics during the development and disintegration of
645 mycobacterial granulomas. Immunity. 2008;28(2):271-84. Epub 2008/02/12. doi:
646 10.1016/j.immuni.2007.12.010. PubMed PMID: 18261937; PubMed Central PMCID:
647 PMCPMC2390753.
648 41. Bouwens L, Baekeland M, De Zanger R, Wisse E. Quantitation, tissue
649 distribution and proliferation kinetics of Kupffer cells in normal rat liver. Hepatology.
650 1986;6(4):718-22. Epub 1986/07/01. PubMed PMID: 3733004.
651 42. Sleyster EC, Knook DL. Relation between localization and function of rat
652 liver Kupffer cells. Lab Invest. 1982;47(5):484-90. Epub 1982/11/01. PubMed PMID:
653 6182391.
654 43. Geissmann F, Cameron TO, Sidobre S, Manlongat N, Kronenberg M, Briskin
655 MJ, et al. Intravascular immune surveillance by CXCR6+ NKT cells patrolling liver
656 sinusoids. PLoS Biol. 2005;3(4):e113. Epub 2005/04/01. doi:

657 10.1371/journal.pbio.0030113. PubMed PMID: 15799695; PubMed Central PMCID:
658 PMCPMC1073691.
659 44. Weber M, Hauschild R, Schwarz J, Moussion C, de Vries I, Legler DF, et al.
660 Interstitial dendritic cell guidance by haptotactic chemokine gradients. Science.
661 2013;339(6117):328-32. Epub 2013/01/19. doi: 10.1126/science.1228456. PubMed
662 PMID: 23329049.
663 45. Matsuda JL, Gapin L, Sidobre S, Kieper WC, Tan JT, Ceredig R, et al.
664 Homeostasis of V alpha 14i NKT cells. Nat Immunol. 2002;3(10):966-74. Epub
665 2002/09/24. doi: 10.1038/ni837. PubMed PMID: 12244311.
666 46. Davis JM, Ramakrishnan L. The role of the granuloma in expansion and
667 dissemination of early tuberculous infection. Cell. 2009;136(1):37-49. Epub
668 2009/01/13. doi: 10.1016/j.cell.2008.11.014. PubMed PMID: 19135887; PubMed
669 Central PMCID: PMCPMC3134310.
670 47. Egen JG, Rothfuchs AG, Feng CG, Horwitz MA, Sher A, Germain RN.
671 Intravital imaging reveals limited antigen presentation and T cell effector function in
672 mycobacterial granulomas. Immunity. 2011;34(5):807-19. Epub 2011/05/21. doi:
673 10.1016/j.immuni.2011.03.022. PubMed PMID: 21596592; PubMed Central PMCID:
674 PMCPMC3164316.
675 48. Flugge AJ, Timmis J, Andrews PS, Moore JW, Kaye PM. Modelling and
676 simulation of granuloma formation in visceral leishmaniasis. Evolutionary
677 Computation, 2009 CEC '09; IEEE Congress 20092009. p. 3052 - 9.
678 49. Beattie L, Sawtell A, Mann J, Frame TC, Teal B, de Labastida Rivera F, et al.
679 Bone marrow-derived and resident liver macrophages display unique transcriptomic
680 signatures but similar biological functions. J Hepatol. 2016;65(4):758-68. Epub

681 2016/06/06. doi: 10.1016/j.jhep.2016.05.037. PubMed PMID: 27262757; PubMed
682 Central PMCID: PMCPMC5028381.
683 50. Amprey JL, Im JS, Turco SJ, Murray HW, Illarionov PA, Besra GS, et al. A
684 subset of liver NK T cells is activated during Leishmania donovani infection by
685 CD1d-bound lipophosphoglycan. J Exp Med. 2004;200(7):895-904. Epub
686 2004/10/07. doi: 10.1084/jem.20040704. PubMed PMID: 15466622; PubMed Central
687 PMCID: PMCPMC2213292.
688 51. Robert-Gangneux F, Drogoul AS, Rostan O, Piquet-Pellorce C, Cayon J,
689 Lisbonne M, et al. Invariant NKT cells drive hepatic cytokinic microenvironment
690 favoring efficient granuloma formation and early control of Leishmania donovani
691 infection. PLoS One. 2012;7(3):e33413. Epub 2012/03/30. doi:
692 10.1371/journal.pone.0033413. PubMed PMID: 22457760; PubMed Central PMCID:
693 PMCPMC3310876.
694 52. Gasteiger G, Fan X, Dikiy S, Lee SY, Rudensky AY. Tissue residency of
695 innate lymphoid cells in lymphoid and nonlymphoid organs. Science.
696 2015;350(6263):981-5. Epub 2015/10/17. doi: 10.1126/science.aac9593. PubMed
697 PMID: 26472762; PubMed Central PMCID: PMCPMC4720139.
698 53. Robinette ML, Fuchs A, Cortez VS, Lee JS, Wang Y, Durum SK, et al.
699 Transcriptional programs define molecular characteristics of innate lymphoid cell
700 classes and subsets. Nat Immunol. 2015;16(3):306-17. Epub 2015/01/27. doi:
701 10.1038/ni.3094. PubMed PMID: 25621825; PubMed Central PMCID:
702 PMCPMC4372143.
703 54. Juno JA, Keynan Y, Fowke KR. Invariant NKT cells: regulation and function
704 during viral infection. PLoS Pathog. 2012;8(8):e1002838. Epub 2012/08/24. doi:

705 10.1371/journal.ppat.1002838. PubMed PMID: 22916008; PubMed Central PMCID:
706 PMCPMC3420949.
707 55. Mattarollo SR, West AC, Steegh K, Duret H, Paget C, Martin B, et al. NKT
708 cell adjuvant-based tumor vaccine for treatment of myc oncogene-driven mouse B-
709 cell lymphoma. Blood. 2012;120(15):3019-29. Epub 2012/08/31. doi: 10.1182/blood-
710 2012-04-426643. PubMed PMID: 22932803; PubMed Central PMCID:
711 PMCPMC3557399.
712 56. Mussai F, De Santo C, Cerundolo V. Interaction between invariant NKT cells
713 and myeloid-derived suppressor cells in cancer patients: evidence and therapeutic
714 opportunities. J Immunother. 2012;35(6):449-59. Epub 2012/06/28. doi:
715 10.1097/CJI.0b013e31825be926. PubMed PMID: 22735803.
716 57. Pilones KA, Aryankalayil J, Demaria S. Invariant NKT cells as novel targets
717 for immunotherapy in solid tumors. Clin Dev Immunol. 2012;2012:720803. Epub
718 2012/11/03. doi: 10.1155/2012/720803. PubMed PMID: 23118781; PubMed Central
719 PMCID: PMCPMC3483734.
720 58. Gonzalez-Aseguinolaza G, de Oliveira C, Tomaska M, Hong S, Bruna-
721 Romero O, Nakayama T, et al. alpha -galactosylceramide-activated Valpha 14 natural
722 killer T cells mediate protection against murine malaria. Proc Natl Acad Sci U S A.
723 2000;97(15):8461-6. Epub 2000/07/19. PubMed PMID: 10900007; PubMed Central
724 PMCID: PMCPMC26970.
725 59. Chackerian A, Alt J, Perera V, Behar SM. Activation of NKT cells protects
726 mice from tuberculosis. Infect Immun. 2002;70(11):6302-9. Epub 2002/10/16.
727 PubMed PMID: 12379709; PubMed Central PMCID: PMCPMC130331.
728 60. Albergante L, Timmis J, Beattie L, Kaye PM. A Petri net model of
729 granulomatous inflammation: implications for IL-10 mediated control of Leishmania

730 donovani infection. PLoS Comput Biol. 2013;9(11):e1003334. Epub 2013/12/24. doi:
731 10.1371/journal.pcbi.1003334. PubMed PMID: 24363630; PubMed Central PMCID:
732 PMCPMC3867212.
733

734 **Figure Legends**

735 **Figure 1. *L. donovani* infection induces transactivation of Kupffer cells for**
736 **chemokine production**

737 (**A**) Heat map showing chemokine mRNA abundance in flow sorted Kupffer cells
738 from naïve mice (control) and from KCs isolated from infected mice and separated
739 into those containing parasites ("infected") and those that do not contain parasites
740 ("inflamed"). KC isolation was performed at 2h and 12h post infection, with matched
741 controls. Lanes numbered 1-4 indicates separate sorts. The gating strategy for
742 separating "infected" from "inflamed" KCs is provided in Figure 3 of reference 31. (**B**
743 and **C**) Two modeling scenarios were generated. In scenario 1 (panel B), only
744 infected KCs produce sufficient chemokine to attract and retain NKT cells. In
745 scenario 2 (panel C) both infected and inflamed KCs produce chemokines to attract
746 NKT cells, although only infected KCs have the ability to retain these through
747 cognate interactions.
748

749 **Figure 2. Overview of the liver agent based model**

750 (**A**) A simulated sinusoidal network was constructed in quasi-2D space using a
751 sinusoidal structure generation algorithm (see **Supplemental Experimental**
752 **Procedures**). A drain node representing the portal vein (black) is placed in the centre
753 of a 2D space with six surrounding entry nodes representing the portal triads (green),
754 forming an irregular hexagon layout (i). Sinusoids (red) are grown from entry nodes
755 to the drain node (ii). Additional entry nodes created around original entry nodes
756 conceptual form a portal triad (iii), allow additional sinusoids to be grown (iv).
757 Additional sinusoid branches are added between existing sinusoids (v).
758 Execution of the algorithm is shown in **Movie S1.** (**B**) Node structure of the model

underlying KC placement and chemokine diffusion. Nodes are populated or not with a single KC, and may attract NKT cells to that node. Chemokines exert their effect by "diffusing" across nodes. For further details, see text and **Supplementary Experimental Procedures**. (**C**) Snapshot of 2-photon image of liver from (mT/mG x lysMcre)$_{F1}$ mice, showing sinusoids (red) and KCs (green).

**Figure 3. Response landscapes for parasite-induced KC activation with and without KC activation in trans.**

(**A-D**) Two-at-a-time (TAT) parameter analysis showing the effect on total KC stimulation time (A, C) and on % inflammatory foci (B and D) of modifying either cumulative time to activate KCs and parasite-induced activation time (A and B) or cumulative time to activate KCs and bystander activation time (C and D). For further details, see **Supplementary Experimental Procedures**.

**Figure 4. Expansion of NKT Cells promotes granuloma formation**

(**A**) Alternate hypotheses for impact of increasing NKT cell number. (**B**) Increasing NKT cells in silico leads to greater percentages of KCs that form an inflammatory focus, when qualified at 4, 6 and 8 cells. (**C - E**) Absolute numbers of NKT (C), NK (D) and T cells (E) in naïve and infected mice with or without administration of rIL-15. Results are pooled from two independent experiments and represent mean±SEM (n=10 mice per group). *P<0.05, **P<0.01, ***P<0.001, by paired Students t-test. (**F**) Percentage of infected KCs with surrounding granuloma in control and rIL-15-treated infected mice. **P<0.01 (n=10 mice). (**G** and **H**) Heterogeneity of granulomas comparing infected (G) and rIL-15-treated (H) mice infected with

784 TdTomato-*L. donovani* (red). Sections were stained using F4/80 (green) and

785 counterstained with DAPI (blue).

786

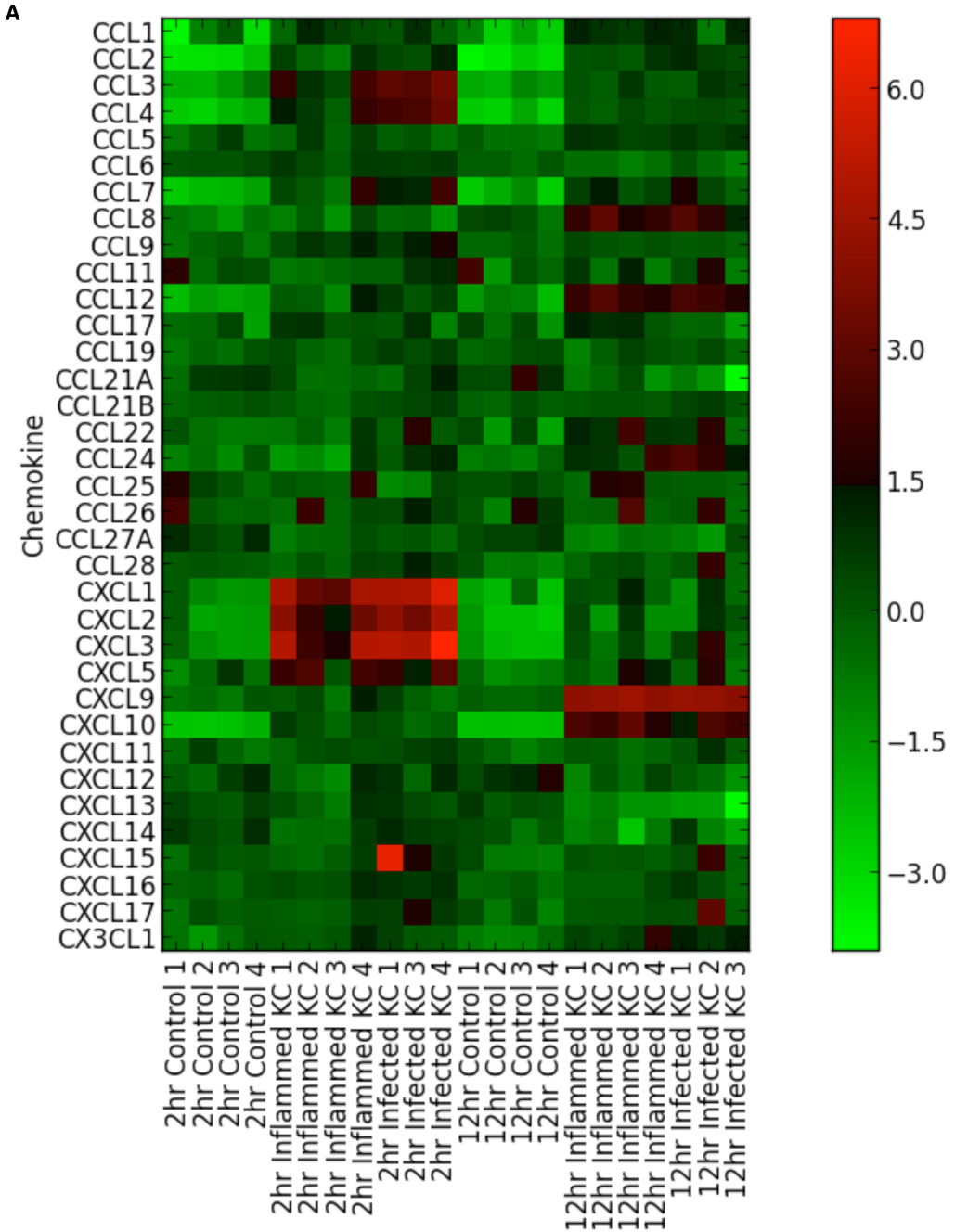
A
Chemokine
CCL1
CCL2
CCL3
CCL4
CCL5
CCL6
CCL7
CCL8
CCL9
CCL11
CCL12
CCL17
CCL19
CCL21A
CCL21B
CCL22
CCL24
CCL25
CCL26
CCL27A
CCL28
CXCL1
CXCL2
CXCL3
CXCL5
CXCL9
CXCL10
CXCL11
CXCL12
CXCL13
CXCL14
CXCL15
CXCL16
CXCL17
CX3CL1
2hr Control 1
2hr Control 2
2hr Control 3
2hr Control 4
2hr Inflammed KC 1
2hr Inflammed KC 2
2hr Inflammed KC 3
2hr Inflammed KC 4
2hr Infected KC 1
2hr Infected KC 3
2hr Infected KC 4
12hr Control 1
12hr Control 2
12hr Control 3
12hr Control 4
12hr Inflammed KC 1
12hr Inflammed KC 2
12hr Inflammed KC 3
12hr Inflammed KC 4
12hr Infected KC 1
12hr Infected KC 2
12hr Infected KC 3
6.0
4.5
3.0
1.5
0.0
−1.5
−3.0

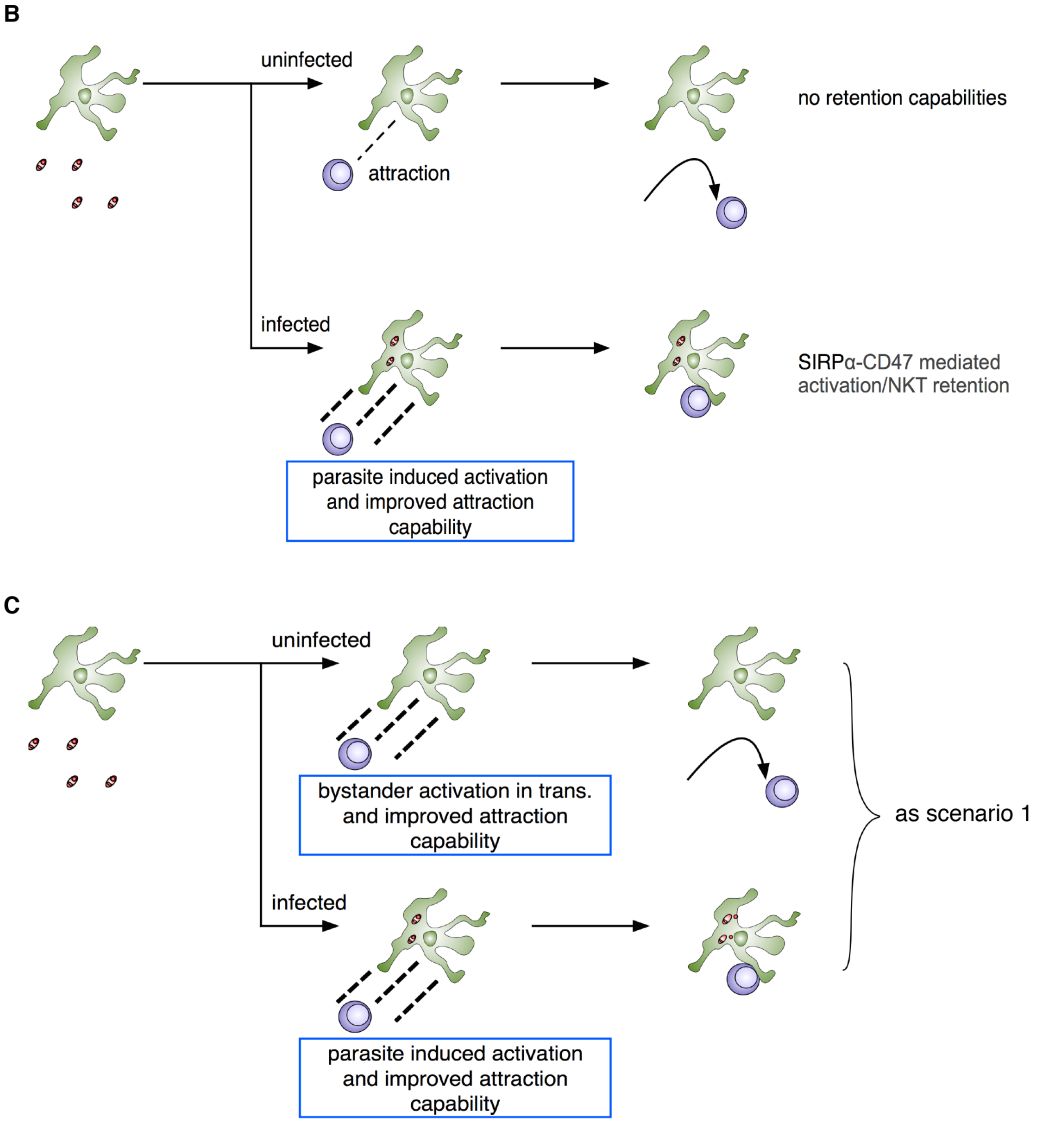
B
uninfected
attraction
no retention capabilities
infected
SIRPα-CD47 mediated
activation/NKT retention
parasite induced activation
and improved attraction
capability
C
uninfected
bystander activation in trans.
and improved attraction
capability
as scenario 1
infected
parasite induced activation
and improved attraction
capability

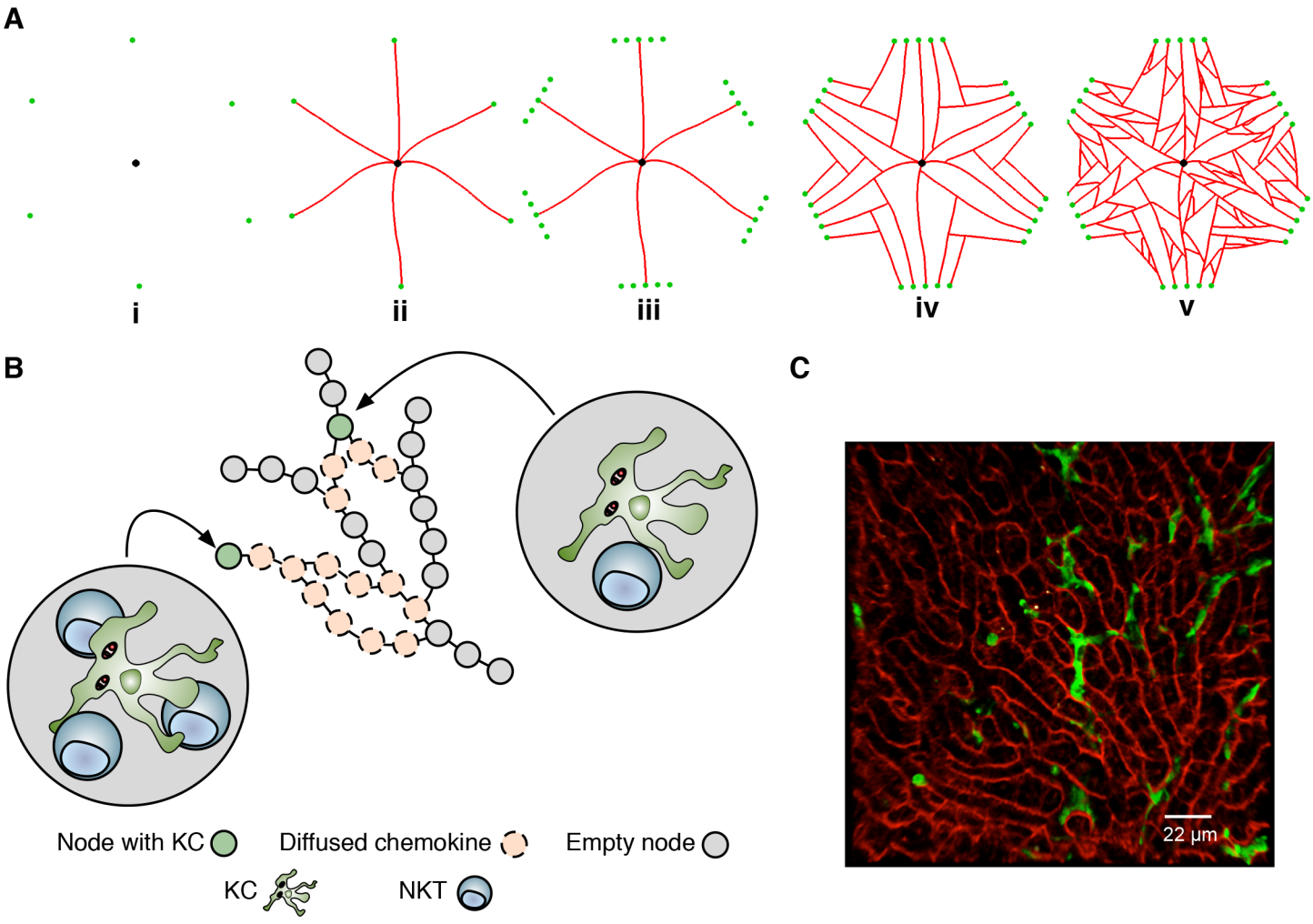
A
i
ii
iii
iv
v
B
Node with KC
Diffused chemokine
Empty node
KC
NKT
C
22 µm

A

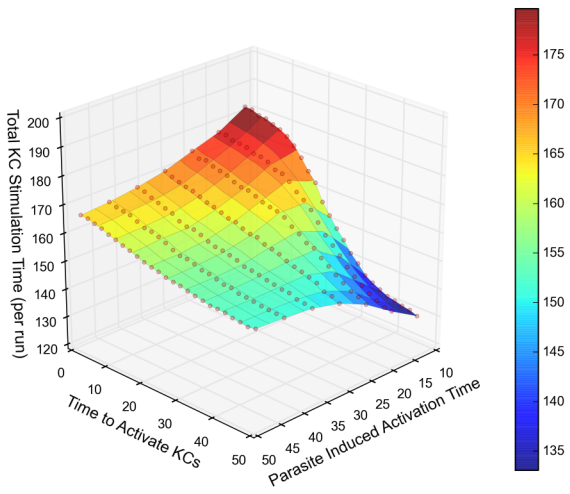
Total KC Stimulation Time (per run)
200
190
180
170
160
150
140
130
120
0
10
20
30
40
50
Time to Activate KCs
50
45
40
35
30
25
20
15
10
Parasite Induced Activation Time
175
170
165
160
155
150
145
140
135

B

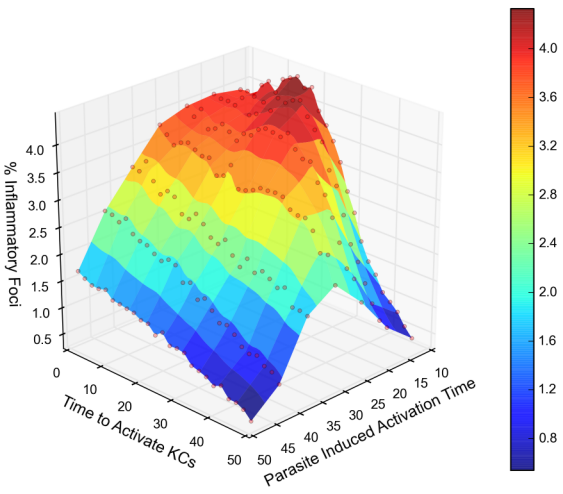
% Inflammatory Foci
4.0
3.5
3.0
2.5
2.0
1.5
1.0
0.5
0
10
20
30
40
50
Time to Activate KCs
50
45
40
35
30
25
20
15
10
Parasite Induced Activation Time
4.0
3.6
3.2
2.8
2.4
2.0
1.6
1.2
0.8

C

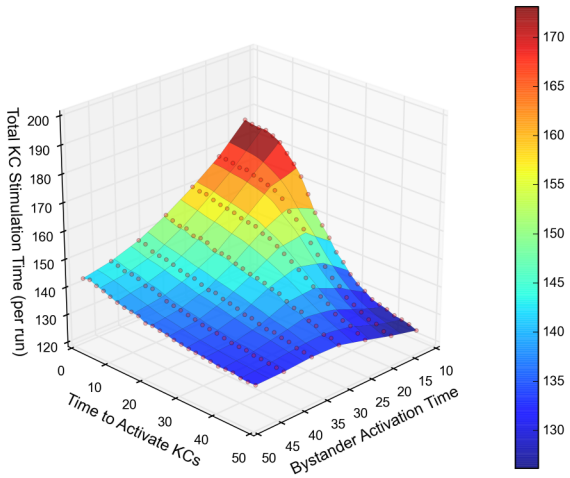
Total KC Stimulation Time (per run)
200
190
180
170
160
150
140
130
120
0
10
20
30
40
50
Time to Activate KCs
50
45
40
35
30
25
20
15
10
Bystander Activation Time
170
165
160
155
150
145
140
135
130

D

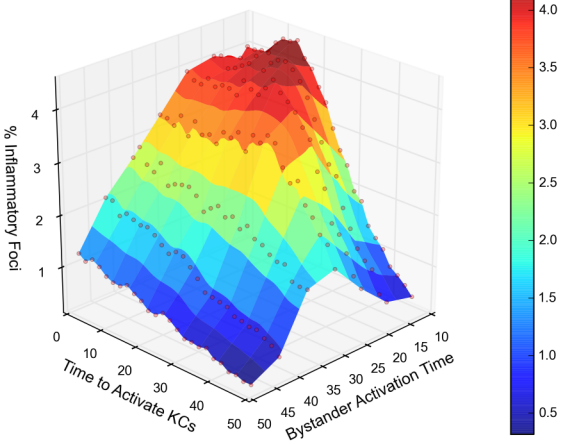
% Inflammatory Foci
4
3
2
1
0
10
20
30
40
50
Time to Activate KCs
50
45
40
35
30
25
20
15
10
Bystander Activation Time
4.0
3.5
3.0
2.5
2.0
1.5
1.0
0.5

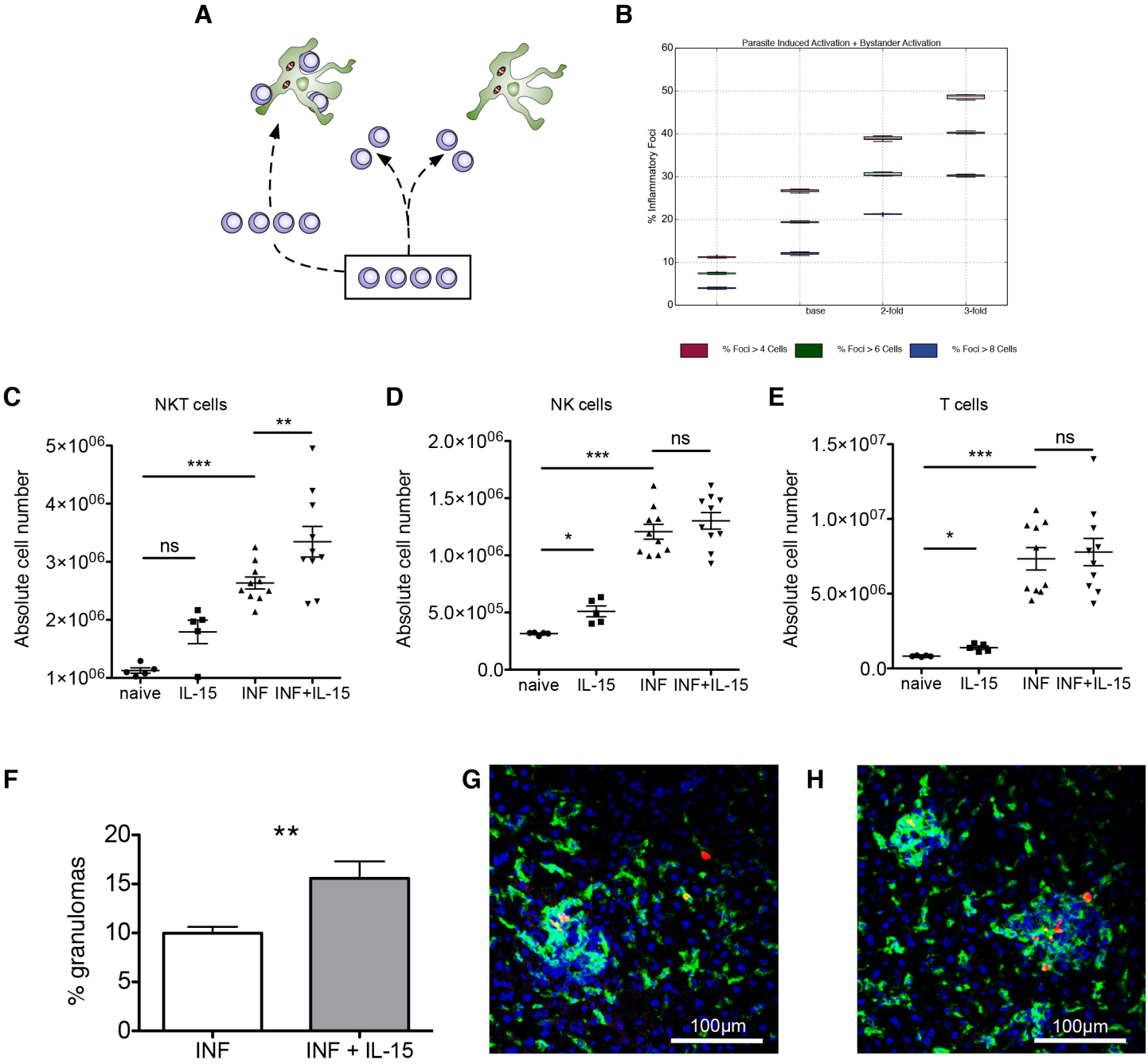
A
B
Parasite Induced Activation + Bystander Activation
% Inflammatory Foci
base
2-fold
3-fold
% Foci > 4 Cells
% Foci > 6 Cells
% Foci > 8 Cells
C
NKT cells
Absolute cell number
naive
IL-15
INF
INF+IL-15
D
NK cells
E
T cells
F
% granulomas
INF
INF + IL-15
G
H
100µm

Supplemental Information

# Macrophage transactivation for chemokine production negatively regulates granulomatous inflammation.

Daniel Moyo[1,2], Lynette Beattie[1*], Paul S Andrews[3], John W J Moore[1], Jon Timmis[3], Amy Sawtell[1], Stefan Hoehme[4], Adam T. Sampson[5], Paul M Kaye[1]

## Supplemental Figures

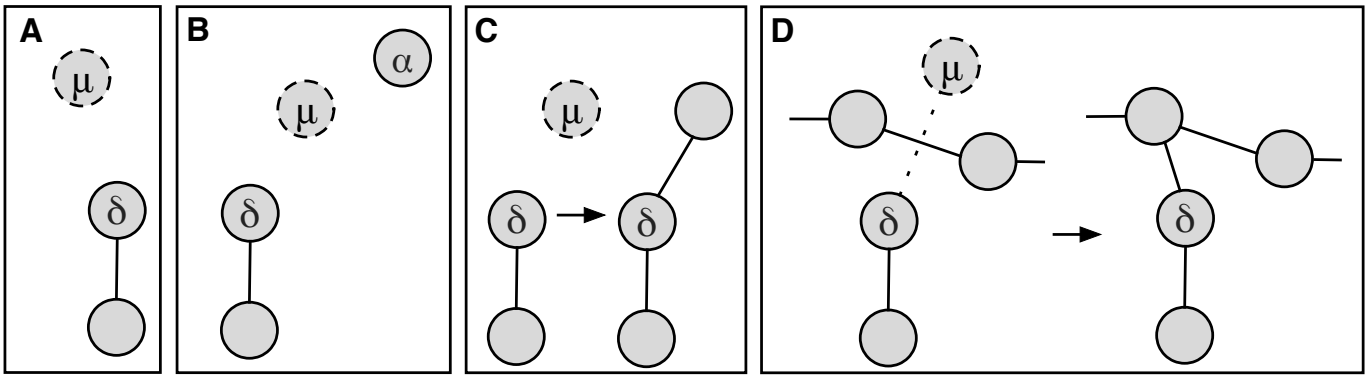


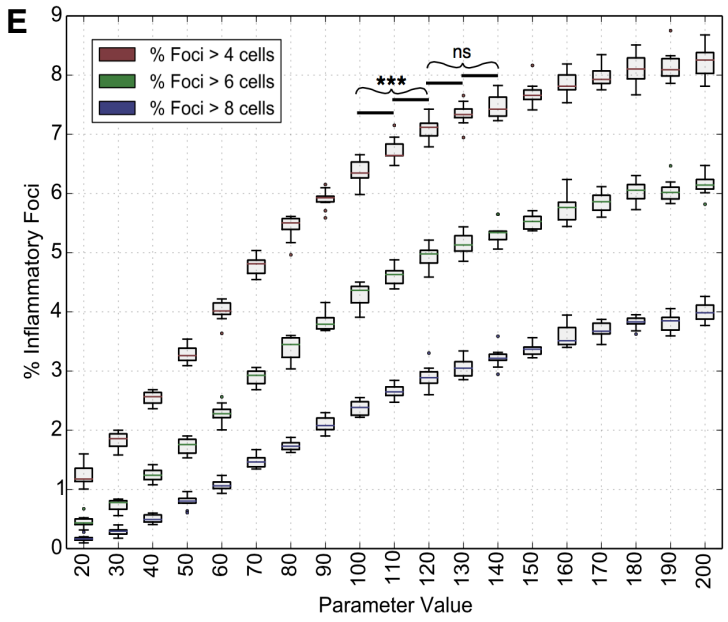


**Figure S1. Related to Figure 2. Generation of Nodes and Edges of a Sinusoid Network.**
(A-D) See Algorithm 1 in Supplemental Experimental Procedures. (E) Effect on percentage inflammatory foci qualified at 4, 6 and 8 cells, when modifying maximum chemokine diffusion distance.

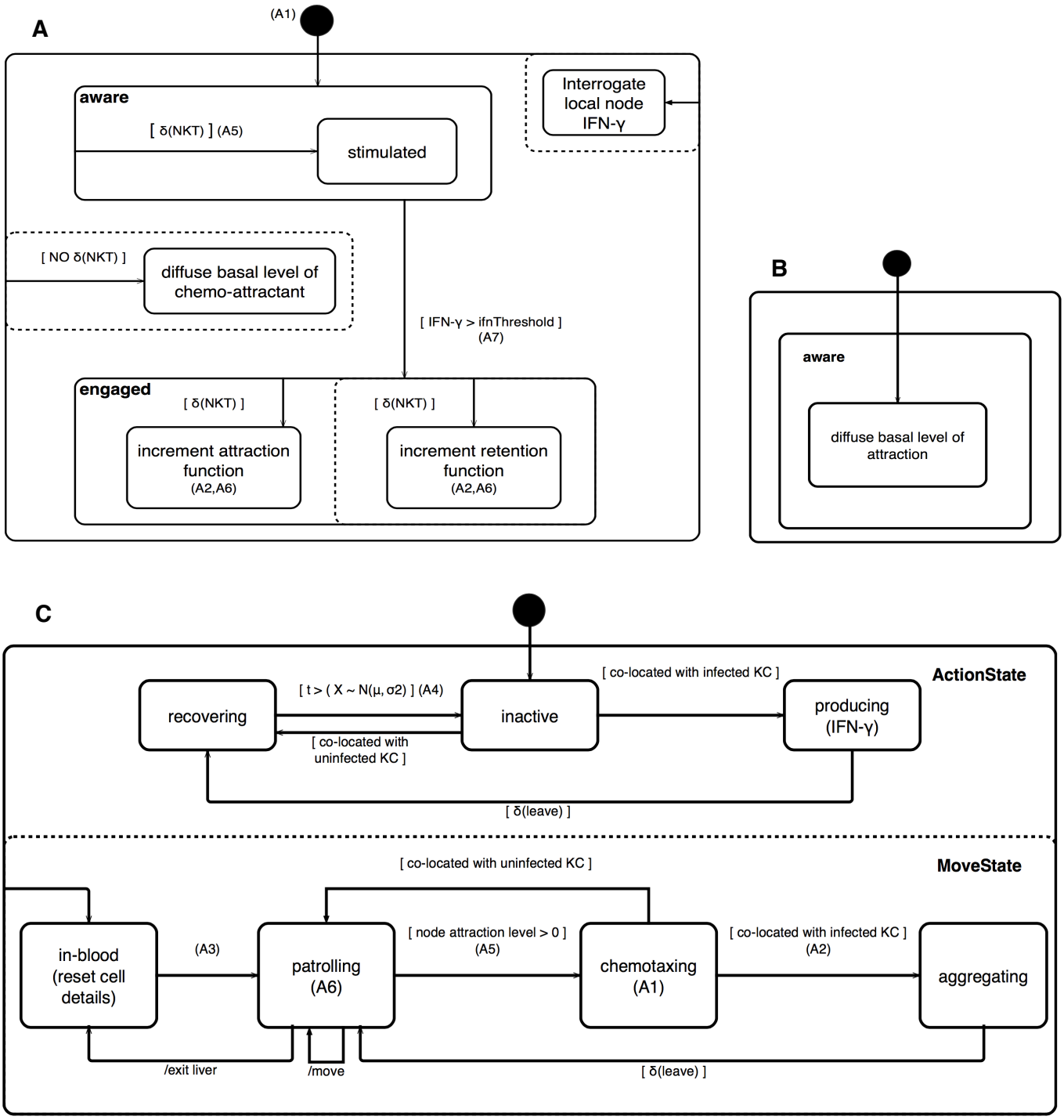


**Figure S2. Related to Figure 2. State-diagrams for Kupffer cell and NKT cell behaviors.**
(A) Infected Kupffer Cell; (B) uninfected Kupffer Cell; (C) NKT cell. See State Transition Diagrams in Supplemental Experimental Procedures.

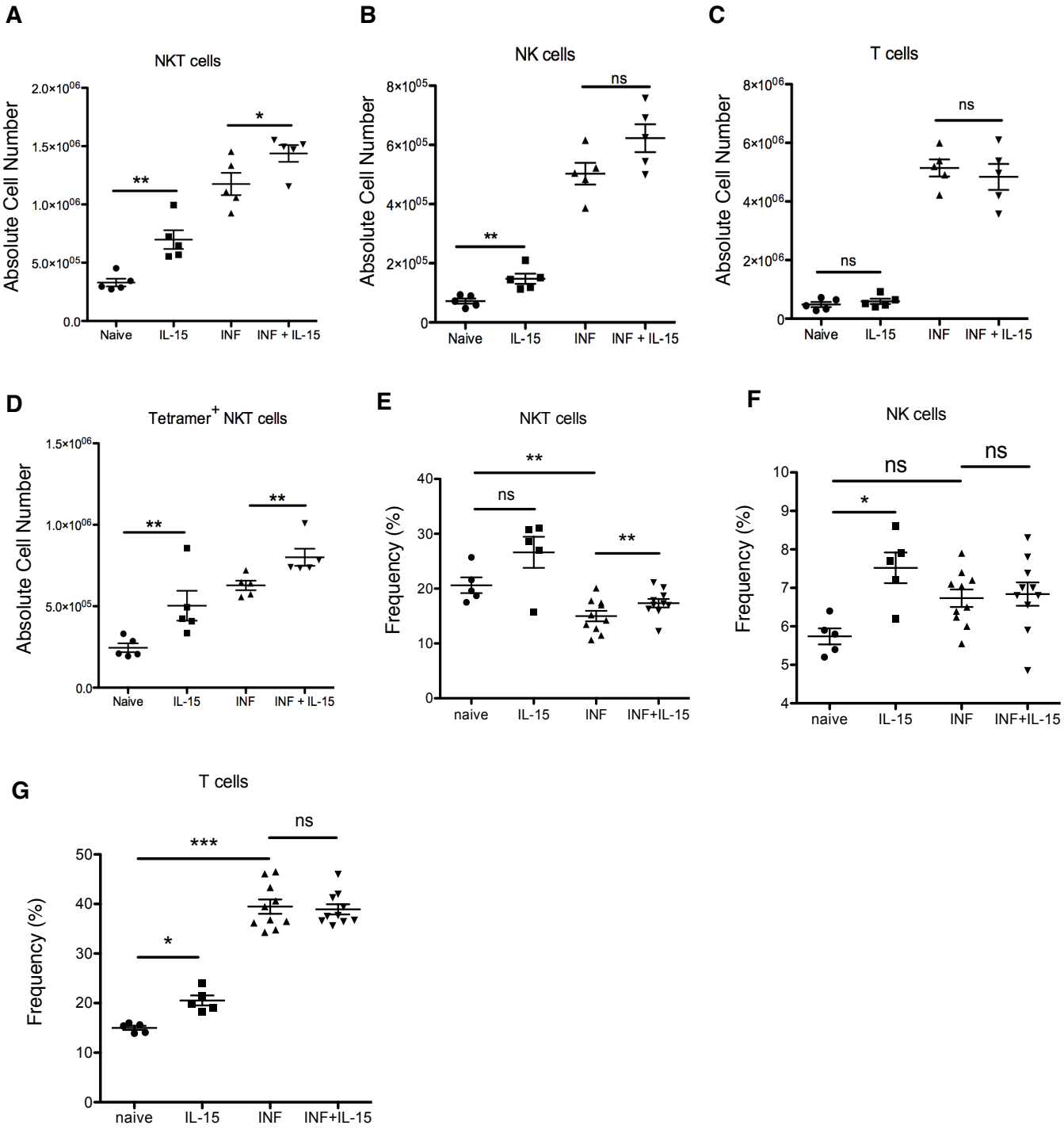


**Figure S3. Related to Figure 4. IL-15 Promotes NKT Cell Expansion.**

(A) Absolute cell numbers for NKT, (B) NK and (C) T cells, and (D) CD1d tetramer+ NKT cells for naïve, IL-15 treated naïve (IL-15), infected (INF) and IL-15 pre-treated infected (INF+IL-15) mice. (E) Relative frequency of NKT, (F) NK and (G) T cells for naïve, IL-15 treated naïve (IL-15), infected (INF) and IL-15 pre-treated infected (INF+IL-15) mice. Results are depicted as mean ± SEM of 5 mice per group. *P≤0.05, **P≤0.01 paired Students t-test.

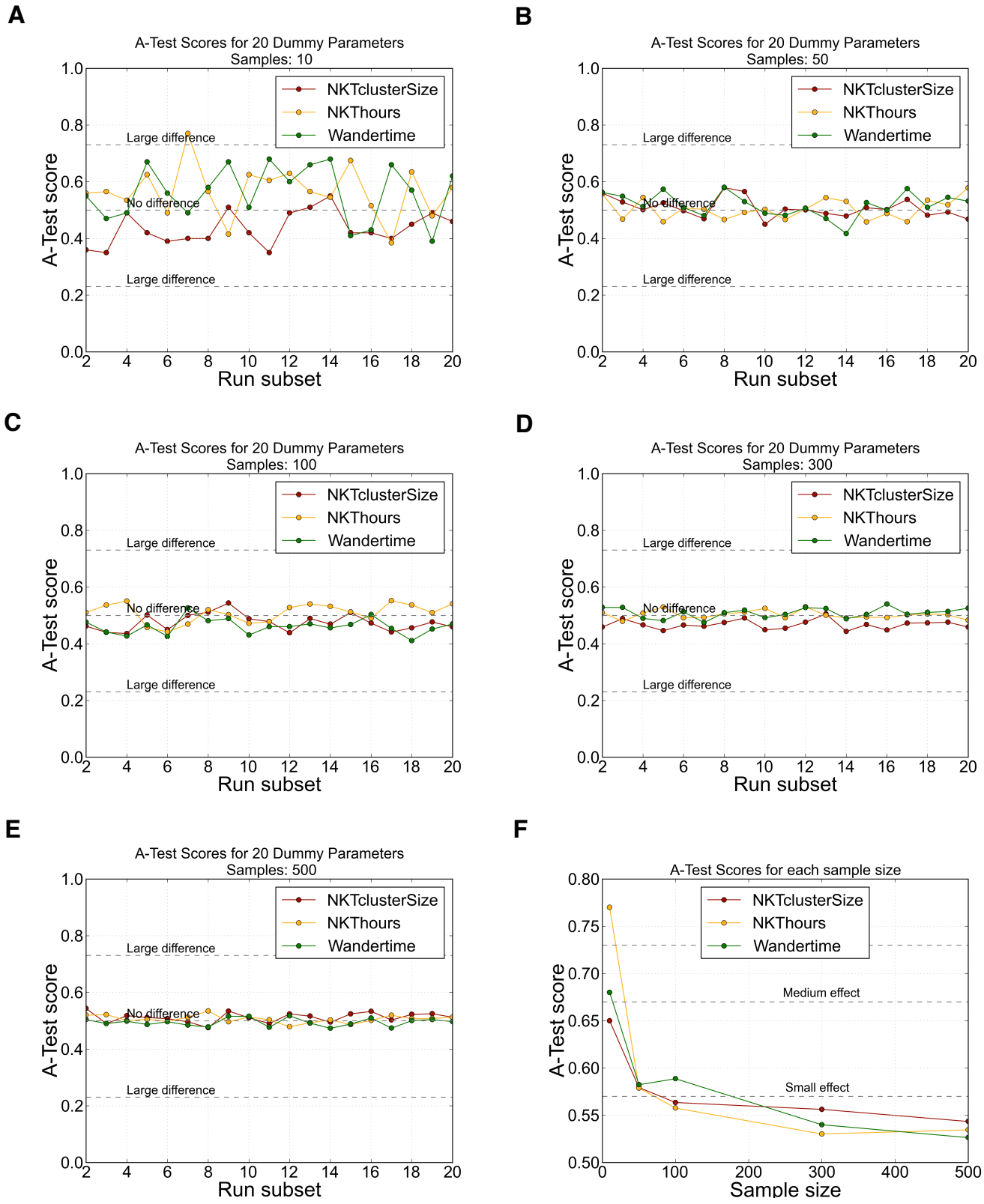


**Figure S4. Related to Figure 2. Aleatory Analysis Determines a Minimum of 300 Simulation Runs per Experiment.**
A-test (Vargha and Delaney, 2000) scores for three simulation output measures across sample sizes of (A) 10, (B) 50, (C) 100, (D) 300 and (E) 500, illustrating that greater than 300 simulation runs are needed to capture the variation in output results and mitigate uncertainty, summarized in (F).

# Supplemental Tables

| **Biological Parameters** | **Value** | **Source** |
|---|---|---|
| NKT cell velocity in the sinusoids | 10-20$\mu$m/minute | (Geissmann et al., 2005) |
| NKT cell numbers in a section of mouse liver lobule | $\sim$49($\sim$1:3 ratio with KCs) | Derived from (Lee et al., 2010) and unpublished data |
| Kupffer cell numbers per gram | 14-20 x $10^{6}$/g | (Bouwens et al., 1986) |
| Infected KCs at 2 hours | $\sim$23% | Unpublished data |
| KCs per lobule section | $\sim$146 | Unpublished data |
| Non-branched segment length | 43.1 $\pm$ 2.25 $\mu$m | (Höhme et al., 2010) |
| Mean branching angles of sinusoids | 32.5$^{\circ}$ $\pm$ 11.2$^{\circ}$ | (Höhme et al., 2010) |
| KC spatial distribution | Percentages:<br>Periportal (PP) - 43<br>Midzonal (MZ) - 28<br>Centrilobular (CV) - 29<br>Ratios: 4(PP), 3(MZ), 2(CV) | (Bouwens et al., 1986; Sleyster and Knook, 1982) |

**Table S1. Related to Figure 2. Table of biological parameters used for calibration.**

| | Domain | Platform | Justification |
|---|---|---|---|
| KC_A1 | | Infected KCs are infected at initiation of the simulation, t(0). | KCs rapidly phagocytose parasites. We are not investigating conditions pre-infection. |
| KC_A2 | | Infected KCs can recruit and retain cells. | Unpublished data. |
| KC_A3 | | Uninfected KCs can only recruit cells. | Unpublished data. |
| KC_A4 | KCs are immobile | KCs have no movement rules | (Lee et al., 2010) |
| KC_A5 | KC retention of NKT cells is probabilistic, mediated by SIRP-a - CD47 interactions and local IFN-g concentration. | Cognate interactions occur when two cells are co-located on the same node and are not modeled explicitly. Retention is modeled probabilistically using a function modified by local IFN-g level | (Beattie et al., 2010; Svensson et al., 2005) |
| KC_A6 | NKT produced IFN-g affects KC attractive chemokine production. | Retentive chemokine level increases in-line with local IFN-g level and increases the diffusion distance of attractive chemokine linearly. Retentive chemokine diffusion distance can decay. | Simplification, no experimental data available. |
| KC_A7 | There is a threshold level of stimulation required to activate a KC. | KCs will not transition to an engaged state until a threshold level of IFN-g is reached. | To facilitate implementation, no experimental data available. |
| NKT_A1 | NKT cells respond to chemo- attractant | NKT cells under chemotaxis, when presented with two or more attraction gradients, will choose a direction based on attractive chemokine strength. | To facilitate implementation, no experimental data available. |
| NKT_A2 | NKT cells interact with KCs | NKT cells will interact with the first infected KC they encounter whilst in chemotaxis. | To facilitate implementation, no experimental data available. |
| NKT_A3 | | The NKT cell population of the lobule section remains constant; cells exiting the environment will enter as new cells via an entry point. | |
| NKT_A4 | NKT cells are capable of becoming anergic | NKT cells are refractive to stimulation and take a period of time to recover after stimulating and leaving a KC. | (Iyoda et al., 2010) |
| NKT_A5 | | NKT cells will respond immediately to a chemokine signal. | To facilitate implementation, no experimental data available. |
| NKT_A6 | NKT cells can walk the sinusoids and switch direction probabilistically NKT cells perform a random walk of the tree- node structure, and a probability governs their | NKT cells perform a random walk of the tree-node structure, and a probability governs their ability to turn in the sinusoids at random. | (Geissmann et al., 2005) |
| C_A1 | Attractive chemokines flow in the same direction as blood would. | Attraction diffuses downstream of infected KCs towards the central vein. | Chemotaxis in 3D environments is poorly understood (Haessler et al., 2011) |
| C_A2 | | Strength of attractive chemokine is a function of distance from source, calculated using a simplified Ficks Law of diffusion. | To facilitate implementation. |
| C_A3 | | Chemokine growth is calculated using a sigmoid function. | To facilitate implementation, no experimental data available. |

**Table S2. Related to Figure 2. Modelling Assumptions.** Statement of assumptions made regarding the underlying biological domain (domain) and how we have abstracted this information in the engineered simulation (platform). Assumptions labeled KC_ relate to Kupffer Cells, NKT_ to NKT Cells, and C_ to chemokines. Assumptions make it possible to model when data is limited or there is a gap in understanding or the literature.

| Parameter | | Value | Units | Description | Source |
|---|---|---|---|---|---|
| Simulation | p_numInfectedKCs | 33 | cells | Number of infected kupffer cells in a π*(284μm)^2 sectional area of sinusoid. | Calibrated to unpublished data |
| | p_numUninfected | 113 | cells | Number of uninfected kupffer cells in a π*(284μm)^2 sectional area of sinusoid. | |
| | p_numNKTs | 49 | cells | Number of NKT cells in a π*(284μm)^2 sectional area of sinusoid. | Calibrated to unpublished data and (Lee et al., 2010)·(Geissmann et al., 2005) |
| Chemokine | p_chemoAttract | 43200 | iterations | Stimulation time required to reach maximum attractive chemokine concentration. | No biological equivalent; explored and chosen through parameter sensitivity analysis |
| | p_chemoRetain | 172800 | iterations | Interaction time required to reach maximum retentive chemokine concentration. | |
| | p_chemoIFN | 172800 | iterations | Interaction time required to reach activate infected KCs. | |

| Parameter | | Value | Units | Description | Source |
|---|---|---|---|---|---|
| NKT cell | p_turnProb | 0.005 | probability | Probability that an NKT cell will reverse direction in the sinusoids. | No biological equivalent; explored and chosen through parameter sensitivity analysis. |
| | p_moveMin | 3 | iterations | Value given to link simulation iterations to NKT cell velocity. | Calibrated to published NKT cell speeds from (Geissmann et al., 2005) |
| | p_moveMax | 6 | | | |
| | p_anergicItns | 3600 | iterations | Time in iterations for an NKT cell to remain unable to stimulate a KC. | No biological equivalent; explored and chosen through parameter sensitivity analysis. |
| | p_escapeItns | 600 | iterations | Time in iterations for an NKT cell to escape the influence of KC produced chemo-attractant. | |
| | p_leaveProb | 0.000265306 | probability | The probability of an interacting NKT cell leaving the location of an infected KC. | |
| | p_minLeaveProb | 0.00005 | probability | To guard against the probabilistic tipping point whereby retention causes cells to never leave. | |
| | p_chemoIFN | 172800 | iterations | Interaction time required to reach maximum attractive chemokine concentration. | |
| Kupffer cell | p_chemoDist | 20 | distance(nodes) | Starting diffusion distance for attractive chemokine. | No biological equivalent; explored and chosen through parameter sensitivity analysis. |
| | p_ratioCV | 0.1 | percentage | Ratio of infected cells in the CV region of the lobule section | Bouwens et al., 1986. Sleyster et al., 1982. |
| | p_ratioMZ | 0.25 | percentage | Ratio of infected cells in the MZ region of the lobule section | |
| | p_ratioPP | 0.65 | percentage | Ratio of infected cells in the PP region of the lobule section | |
| | p_maxDist | 200 | distance(nodes) | Maximum diffusion distance for attractive chemokine. | Calibrated to twice reported max(Weber et al., 2013) |
| | p_ifnThreshold | 0.999 | threshold | Threshold value of IFN-γ required to activate a KC. Chemokine function f(x)→1, therefore a threshold is required. | No biological equivalent |

**Table S3. Related to Figure 2. Simulation Parameters.** Summary of the simulation parameters, descriptions of their purpose, values and any data sources for parameters relating to cell numbers and chemokine functions. All estimated values are based on a comprehensive sensitivity analysis for parameters that have unknown or no clear biological value.

## Supplemental Movies

**Movie S1. Related to Figure2. Sinusoid structure generation algorithm.** Execution of the sinusoid structure generation algorithm at 8x speed. Drain node (cyan), entry nodes (green) and sinusoids (red).

# Supplemental Experimental Procedures

We assume that our sinusoid network exists in a quasi-2D space (we can consider this as a slice through a 3D lobule). We also assume that the lobule structure is roughly hexagonal with a single central vein in the centre and six portal triad areas placed at roughly regular intervals around the central vein. The flow of blood borne cells is assumed to be from portal triads to the central vein, so in the algorithmic description below the central vein is termed a drain node, and the portal triad regions deemed entry nodes.

Algorithm 1 describes how the nodes and edges of the sinusoid network are generated, whilst Algorithm 2 describes how the overall sinusoid network (the lobule) is generated using Algorithm 1. Höhme et al. (2010) provide us with the following statistics that guide Algorithm 2:

- Average length between central vein and portal triad = 284$\mu$m;
- Average length of a non-branched sinusoid = 43.1$\mu$m;
- Average angle between branching sinusoids = 32.5°.

## Algorithm 1: Sinusoid branch generation

1. A potential new node ($\mu$) is generated 1$\mu$m from the current node ($\delta$)
   (a) If we are within range of an attracting node ($\alpha$) then $\mu$ is generated in the direction of $\alpha$ (see Figure S4(B)).
   (b) Otherwise $\mu$ is generated based on our current direction with a small random adjustment (see Figure S4(A)).
2. Create a new edge between $\delta$ and another node:
   (a) If the line between $\delta$ and $\mu$ intersects another edge in the sinusoid network, then connect $\delta$ to the closest existing node (see Figure S4(D)).
   (b) Otherwise connect $\delta$ and $\mu$ (see Figure S4(C)).
3. Repeat Steps 1 and 2 until an intersection is detected.

## Algorithm 2: Sinusoid network (lobule) generation

1. A drain node (representing the central vein) is placed in the centre of the 2D space, surrounded by six entry nodes (representing the locations of portal triads) in an irregular hexagon formation (see Figure 2(Ai)). The exact location of the entry nodes is determined stochastically.
2. For each of the six entry nodes a sinusoid branch is grown (see algorithm 1) from the entry node towards the attracting drain node (see Figure 2(Aii)).
3. An additional set of entry nodes is created for each original entry node and aligned with the original node. These additional nodes represent additional sources of blood supply coming out of the portal triad (see Figure 2(Aiii)).
4. For each of the new entry nodes a sinusoid branch is grown (see algorithm 1) from the entry node towards the existing sinusoid structure (see Figure 2(Aiv)).
5. Additional sinusoids are created to connect existing sinusoids (see Figure 2(Av)).
   - Select the longest sinusoid in the structure
   - Select a node in the longest sinusoid and grow a sinusoid (see algorithm 1) to either the left or right at an angle drawn from a normal distribution with a mean of 32.5°.
   - Repeat until the mean sinusoid length of the entire structure reaches 43.1$\mu$m.

## Cell Attraction Dynamics

If we assume an infected KC diffuses chemokine to a downstream node $\alpha$, chemokine strength at $\alpha$ is a function of distance:

$$\lambda/\delta$$

Where:

$\lambda$ is the chemokine strength at the infected node.
$\delta$ is the distance in nodes between the KC and $\alpha$.

Uninfected KCs are unable to modify their attraction diffusion distance from the parameterized minimum (Scenario A only), whereas infected-KC attractive chemokine diffusion distance is variable between a minimum and maximum distance. That distance is calculated as a function of the current level of attractive chemokine at the source KC location:

$$\delta = | \lambda \cdot (\delta\text{max} - \delta\text{min}) |$$

Where:

$\lambda$ is the chemokine strength at the infected node.
$\delta$max is the maximum parameterized diffusion distance.
$\delta$min is the minimum parameterized diffusion distance

The function is floored to the nearest integer and that is used as the updated diffusion distance.

## Cell Retention Dynamics

The equation governing NKT cell retention is:

$$\delta\text{nktleave} = \delta\text{leave} \ \ (\phi \cdot \delta\text{leave})$$

Where:

$\delta$nktleave is the probability of an NKT cell leaving an infection site.
$\delta$leave is the maximum parameterized retention probability.
$\phi$ is the level of retentive chemokine at the infected node.

As the calculated probability will approach zero given suitable conditions, a minimum retention probability is parameterized to ensure that KCs do not become so retentive that NKT cells are then incapable of leaving.

## State-Transition Diagrams

Figure S2 depicts state-transition diagrams using the Unified Modelling Language (UML). These diagrams are the engineering specific (platform) ones used to create the simulator. To improve clarity, various annotations are added to convey information relevant to our modelling context. Arrows denote transitions between states. Square brackets ([]) denote guards for a transition, conditions that must be met before a transition can occur. Dashed lines denote states or behaviours that occur concurrently. Where an assumption number is stated on a diagram, denoted by (An), refer to the relevant cell assumption table. The $\delta()$ notation denotes an interaction that might occur probabilistically, for example a cell-cell interaction.

- **Infected Kupffer Cells** (Figure S2(A)): begin in an aware state and have a minimum level of attractive chemokine and minimum diffusion distance of attraction. If the level of cell-local interferon-gamma produced by NKT cells reaches a threshold (ifnThreshold), infected KCs become engaged. When infected KCs are engaged, if there is sustained interaction with NKTs, indicated by $\delta$(NKT), they will increase their level of attraction and retention.
- **Uninfected Kupffer Cells** (Figure S2(B)): always in an aware state and only diffuse the minimum level of attractive chemokine. They do not interact with NKTs by any other means.
- **NKT cells** (Figure S2(C)): have two state types, ActionStates and MoveStates. The initial ActionState is inactive. If an infected KC is encountered the NKT will begin producing interferon- until probabilistically leaving mediated by the retention level of the KC. If NKT cells encounter uninfected KCs, they will transition to the recovering state. NKTs leave the recovering state after a time sampled from a normal distribution, this time is significantly shorter for NKTs that previously left uninfected KCs, and hence havent been in the producing state. The default NKT cell MoveState is patrolling. Upon sensing a level of attraction, NKT cells will transition to a chemotaxing state. Interaction with an infected KC will cause the NKT to switch to an aggregating state; alternatively an uninfected KC encounter will lead back to a patrolling state. Aggregating NKT cells can transition to patrolling behavior probabilistically. Should NKT cells exit the liver environment, if the entry condition is satisfied, they will emerge from an environment entry point, effectively as another cell.

## Parameterizing and Calibrating the Simulation

A full summary of the biological data available that was used to calibrate the simulation is listed in Table S1, though these are merely the domain specific parameters, and a number of implementation specific parameters are required in order to abstract domain behaviors into executable computer code. A good example of an implementation specific parameter relates to NKT cell speed. NKT cells traverse the sinusoids at 10-20m/minute. In the simulation, this corresponds to 10-20 nodes/minute. Our simulation iterations are in seconds, so for a cell to travel at a maximum speed of 20 nodes/minute it would have to move every 3 simulation iterations (p_moveMin), and a minimum speed of 10 nodes/minute every 6 simulation iterations (p_moveMax). Rather than have individual cell speed remain constant, we allow it to be dynamic within the published biological range. We calculate, probabilistically between p_moveMin and p_moveMax, the number of iterations a cell will remain stationary before its next move. This allows individual cells to speed up and slow down dynamically, yet maintains a normal distribution of cell speeds across the population and within the biologically specified range. The entire list of baseline simulation parameters can be viewed in Table S3. Several parameters have no biological equivalent though are fundamental for the implementation of many behaviors. We performed parameter sensitivity analysis (SA) in order to determine which parameters the simulation is extremely sensitive to, and to establish baseline parameter values. Finally SA allows us to ensure we are always interpreting our results with the knowledge that particular extreme parameter combinations might influence those results.

Each simulated experiment is run across 10 separate structures in order to approximate variance across the set. For each parameter value investigated (or combination of parameter values) per experiment, 500 simulation runs are performed, this number chosen after performing aleatory uncertainty analysis on the simulator. Aleatory analysis can be used to determine the minimum number of replicates runs required to both mitigate the effects of stochasticity on simulation output, and to generate results that cover a representative spectrum of possible system behaviours (Alden et al., 2013). Fig. S3f shows that 300 simulation runs per parameter combination are sufficient to have acceptable uncertainty (small variance between identical sample sizes), though we perform 500 in order to strike a balance between further reducing A-test effect size (Vargha and Delaney, 2000) and maintaining tractable simulated-experiment execution times.

## Supplemental References

Haessler, U., Pisano, M., Wu, M., and Swartz, M.A. (2011). Dendritic cell chemotaxis in 3D under defined chemokine gradients reveals differential response to ligands CCL21 and CCL19. Proceedings of the National Academy of Sciences of the United States of America 108(14), 5614-5619.

Iyoda, T., Ushida, M., Kimura, Y., Minamino, K., Hayuka, A., Yokohata, S., Ehara, H., and Inaba, K. (2010). Invariant NKT cell Anergy is Induced by a Strong TCR-Mediated Signal Plus Co-stimulation. International Immunology 22(11), 905913.

Vargha, A., and Delaney, H. D. (2000). A Critique and Improvement of the "CL" Common Language Effect Size Statistics of McGraw and Wong. Journal of Educational and Behavioral Statistics 25(2), 101132.